OPEN ACCESS

Catalysis & Surface ARTICLE

To dissipate is to stabilize: Mechanical loss in methane hydrates

Yongxiao Qu,[1,3] Qiao Shi,[1,3] Gaoyang Luo,[1] Rui Ma,[2] Zhisen Zhang,[1] Zhiliang Zhang,[2,*] and Jianyang Wu[1,2,*]

*Correspondence: zhiliang.zhang@ntnu.no (Z.Z.); jianyang@xmu.edu.cn (J.W.)

Received: December 17, 2025; Accepted: April 7, 2026; https://doi.org/10.59717/j.xinn-energy.2026.100157

GRAPHICAL ABSTRACT

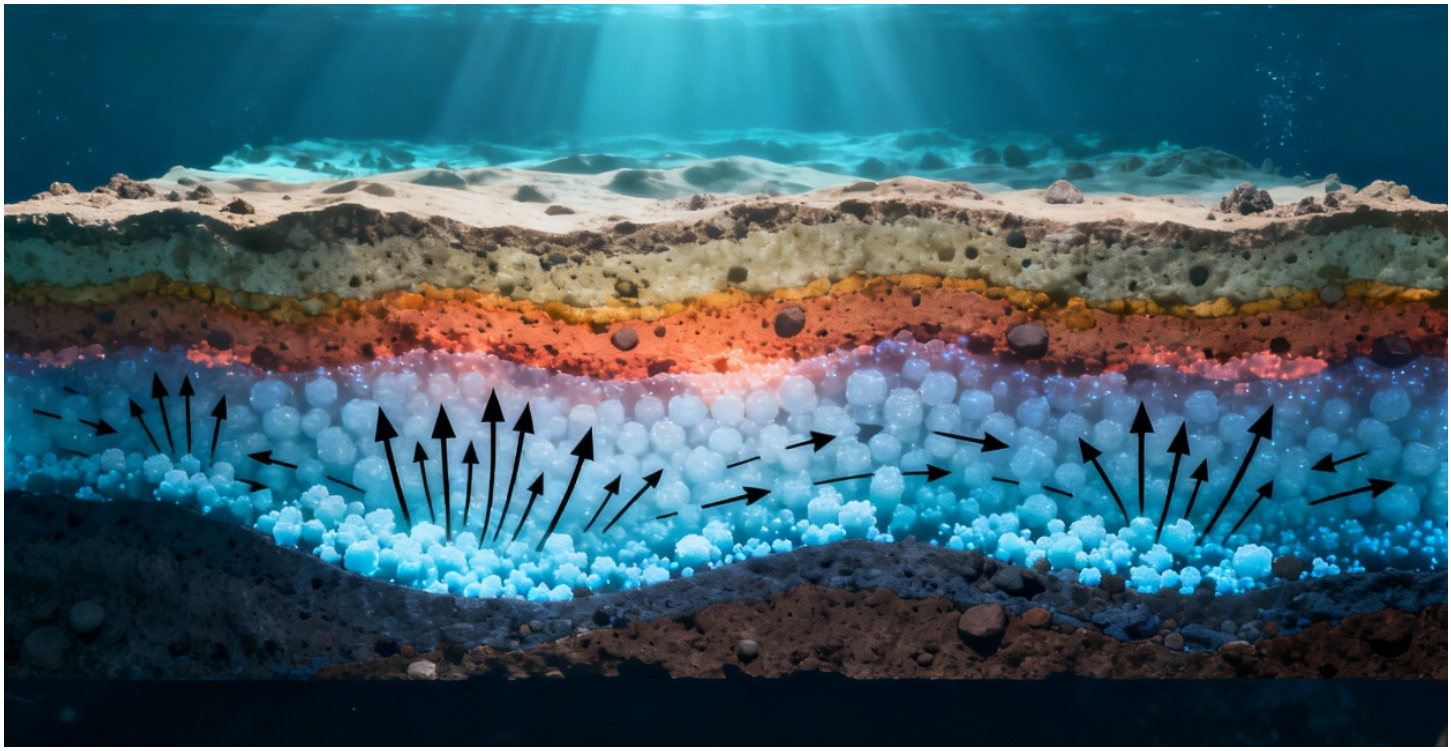

PUBLIC SUMMARY

- Controlled mechanical loss underpins the long-term integrity of methane hydrate reservoirs.
- Grain size and loading frequency dictate elastoplastic fracture or viscoelastic dissipation.
- Measured low-frequency limit explains exceptional natural stability.
- Cage transformations and phase transitions at GBs efficiently release strain energy.
- To Dissipate is to Stabilize: Mechanical Loss in Methane Hydrates

ARTICLE Catalysis & Surface

www.the-innovation.org/the-innovation-energy

To dissipate is to stabilize: Mechanical loss in methane hydrates

Yongxiao Qu,[1,3] Qiao Shi,[1,3] Gaoyang Luo,[1] Rui Ma,[2] Zhisen Zhang,[1] Zhiliang Zhang,[2,*] and Jianyang Wu[1,2,*]

[1]Department of Physics, Research Institute for Biomimetics and Soft Matter, Jiujiang Research Institute and Fujian Provincial Key Laboratory for Soft Functional Materials Research, Xiamen University, Xiamen 361005, China

[2]NTNU Nanomechanical Lab, Norwegian University of Science and Technology (NTNU), Trondheim 7491, Norway

[3]These authors contributed equally

*Correspondence: zhiliang.zhang@ntnu.no (Z.Z.); jianyang@xmu.edu.cn (J.W.)

Received: December 17, 2025; Accepted: April 7, 2026; https://doi.org/10.59717/j.xinn-energy.2026.100157

Citation: Qu Y., Shi Q., Luo G., et al. (2026). To dissipate is to stabilize: Mechanical loss in methane hydrates. *The Innovation Energy* **3**:100157.

Natural gas hydrates (NGHs) represent a vast potential energy resource, yet their mechanical instability under geological or anthropogenic stresses threatens seafloor stability and poses climate risks. Using large-scale molecular dynamics simulations, we demonstrate how ultralow mechanical loss enables long-term stability in polycrystalline methane hydrates under cyclic shear. Our analysis reveals two distinct deformation regimes governed by grain size, temperature, and loading frequency. Under high-frequency, small grained methane hydrates undergo transgranular fracture, whereas large grained methane hydrates deform through elastic kink banding, maintaining structural coherence. Under low-frequency and elevated temperature conditions, which is characteristic of geological settings, the response becomes viscoelastic, with energy dissipation dominated by grain boundary activities including molecular diffusion, cage structure transformations, and sI ↔ sII phase transitions. These grain boundaries, enriched in metastable noncanonical cages, serve as dissipation hotspots where cage restructuring and phase transitions efficiently release strain energy. Crucially, the frequency-dependent mechanical loss follows the Cross model, exhibiting an ultralow loss tangent limit of 0.22 that underpins the exceptional stability of natural hydrate systems. This work establishes a molecular-to-macroscopic framework linking dissipation mechanisms to reservoir-scale stability, providing fundamental insights for assessing hydrate integrity under natural and anthropogenic perturbations.

INTRODUCTION

Natural gas hydrates (NGHs) are non-stoichiometric ice-like crystalline compounds wherein water molecules form hydrogen-bonded (HB) polyhedral cavities under low-temperature and high-pressure conditions. This unique clathrate structure enables methane entrapment while stabilizing the crystalline framework.[1-5] Three primary crystalline structures of NGHs occur in both natural and lab-settings, including sI, sII and sH clathrate hydrates,[2,6] with sI NGH dominating natural deposits across continental margins and in permafrost regions.[7-10] Moreover, the potential occurrence of gas hydrates on extraterrestrial bodies[11-13] expands the relevance of NGH research beyond Earth, hinting at broader planetary implications.

NGHs are prone to destabilization when environmental conditions change due to natural and anthropogenic factors, such as earthquakes or petroleum-related activities, which impose excessive mechanical stress or strain. Large-scale destabilization of NGHs can trigger geological disasters, including submarine landslides, and release methane, which has a significant impact on global climate change.[14,15] Therefore, the mechanical stability of NGHs critically governs seafloor stability, the safety of NGH exploitation, and even planetary evolution,[16,17] attracting considerable research attention. For example, mechanical compression creep experiments on polycrystalline methane hydrates (PMHs) revealed that at temperatures slightly below freezing, the mechanical strength of PMHs can be 20 to 40 times higher than that of ice,[18,19] and PMHs undergo extensive work-hardening, accompanied by a solid-state disproportionation process.[20] Triaxial compression tests of sand-contained methane hydrates (MHs) showed strong time-dependent mechanical behaviors, with creep life predictable via relationships between loading rate and strength.[21-23] Using molecular dynamics (MD) simulations, PMHs under uniaxial tension and compression exhibited pseudo Hall-Petch and pseudo inverse Hall-Petch behaviors in ultimate strength, originating from grain size-induced grain-boundary (GB) accommodation and hydrate phase change.[24] This not only provides molecular insights into the intrinsic mechanism of deformation-induced hydrate dissociation observed in macroscopic experiments but also bridges the gap between microscopic and macroscopic observations, which is a key step in multiscale analysis[24]. In addition, MD simulations of creep loads of PMHs revealed that the mechanical creep responses of PMHs are primarily affected by grain size (d), temperature (T) and static load stress.[25]

The relaxation dynamics and viscoelastic properties of subduction zones play critical roles in assessing and predicting the physical properties of the earthquake cycles,[26,27] and the influence of the deformation mechanism of seafloor sediments on their subduction process is of great significance.[28,29] The seafloor sediments contain massive PMHs in hydrate reservoirs. As a result, the relaxation dynamics and viscoelastic behavior of PMHs are essential for assessing the long-term stability of subduction zones and seafloor sediment-hosted hydrate reservoirs. This is not only helpful for sustainable commercial exploitation of NGHs but also for hydrate-based geological CO_2 storage. Currently, however, there is a lack of information on the viscoelastic properties of NGHs, as well as a lack of understanding of molecular insights into time-dependent viscoelasticity. In polycrystalline metals, microstructural heterogeneity drives internal dissipation, with GB diffusion and viscous sliding as primary energy-dissipation mechanisms across timescales.[30-33] For NGHs, however, it still remains open questions as how to connect macroscopic dissipation with micro/nanoscale deformation mechanisms in PMHs, and mechanical cyclic responses to internal dissipation.

Beyond its fundamental rheological significance, mechanical dissipation in hydrate-bearing materials is also closely related to the practical utilization of NGH resources. During gas production processes such as depressurization, thermal stimulation, or CO_2-CH_4 replacement, hydrate reservoirs are subjected to cyclic stresses and time-dependent deformation, where mechanical loss governs how strain energy is dissipated and redistributed within the sediment framework. These processes can influence reservoir integrity, gas recovery efficiency, and the long-term stability of CO_2 storage in hydrate-bearing sediments, highlighting the importance of understanding dissipative mechanical behavior of NGHs for sustainable energy production and climate mitigation.

Herein, we delve into the dynamic mechanical behaviors of PMHs under cyclic shear loading, identifying two distinct deformation modes governed by d, T and loading frequency (ω). Depending on ω, PMHs exhibit elastoplastic or viscoelastic deformation. Small-grained PMHs fail via transgranular fracture, while large-grained ones undergo intragranular elastic bending deformation, avoiding transgranular fracture and demonstrating robust stability. At low ω and high T, the microstructure and composition of GBs play a crucial role in the mechanics of PMHs, driving a transition from elastic to viscoelastic behavior. PMHs show nonlinear relationships between d and ω and dynamic moduli, with mechanical loss versus ω well-described by the Cross model for non-Newtonian fluids. T- and ω-dependent dynamic moduli reveal time-temperature superposition in mechanical properties. These findings establish the connections between factors of d, T and ω and dynamic mechanical properties of PMHs while elucidating the origins of mechanical loss. This work advances understanding of the dynamic mechanical properties of NGHs, enabling predictions of NGHs reservoir stability under tectonic or anthropogenic disturbances.

MATERIAL AND METHODS

Molecular models of PMHs

The Voronoi tessellation algorithm (VTA) is utilized to construct molecular

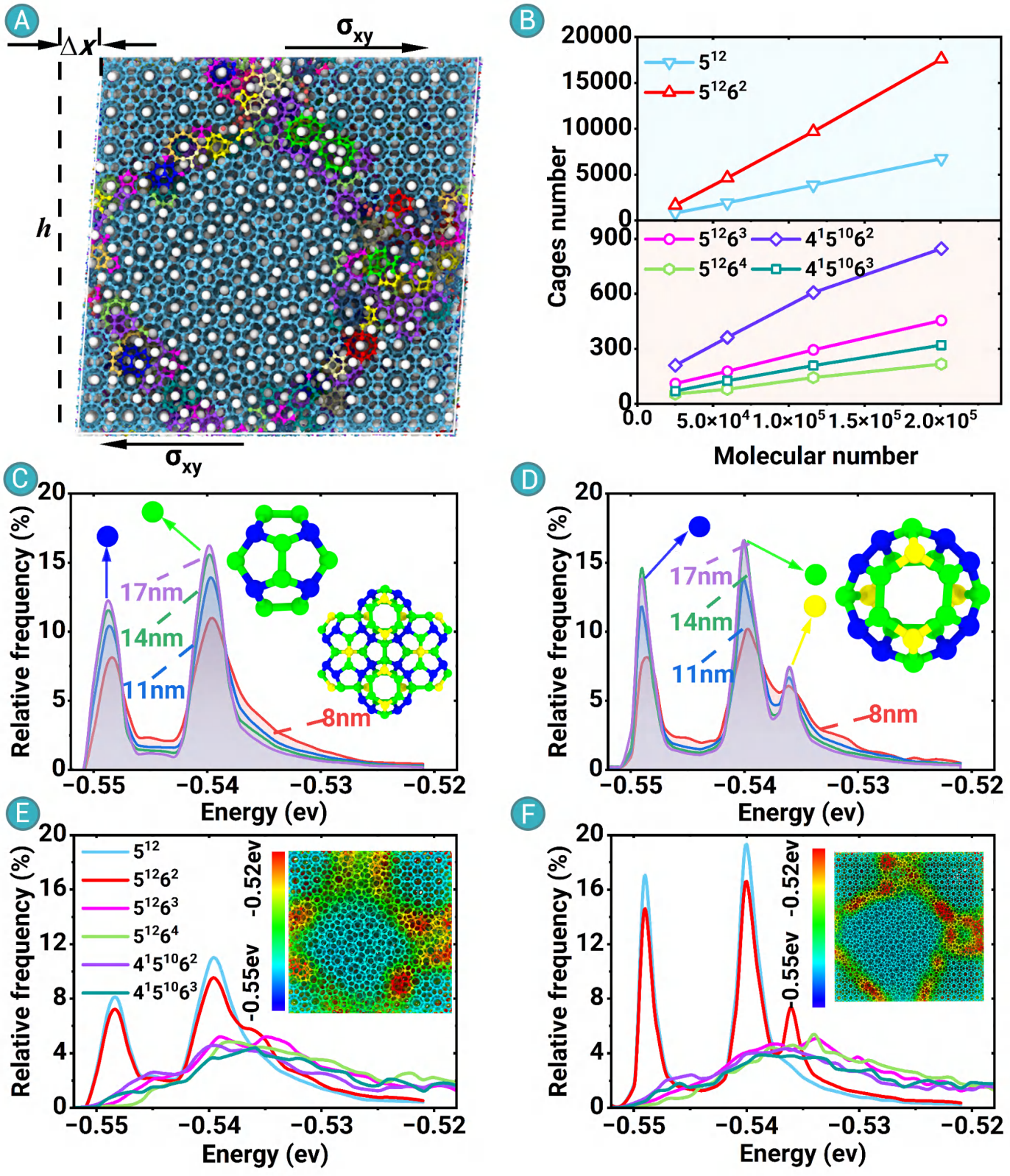

Figure 1. Distribution profiles of potential energy of water molecules (E_w) in polycrystalline methane hydrates (PMHs) (A) Schematic diagram of shear load of PMHs, in which the white balls indicate the methane particles, while the water particles are colored based on the formation type of clathrate cages. (B) Variation in the number of clathrate cages with the number of water molecules or *d*. (C) and (D), Distribution profiles of E_w in 5^{12} and $5^{12}6^2$ cages in PMHs with different *d*, respectively. (E) and (F), Distribution profiles of E_w in clathrate cages of 5^{12}, $5^{12}6^2$, $5^{12}6^3$, $5^{12}6^4$, $4^15^{10}6^2$ and $4^15^{10}6^3$ in PMHs with d = 8 and 14 nm, respectively. The vertical axis represents the relative frequency, defined as the number of water molecules with a given E_w divided by the total number of water molecules.

models of PMH structures.[34] The unit-cell crystalline structure of sI hydrate serves as the seed by VTA to construct PMHs, in which the starting position of oxygen atoms of water molecules and the center of mass of guest methane molecules are derived from the X-ray diffraction data of ethylene oxide hydrate.[35] To examine the effect of *d* on dynamic mechanical properties, PMH samples with d = 8, 11, 14 and 17 nm are constructed, where *d* denotes the edge length of the cubic polycrystalline simulation cell containing four grains generated using the VTA. Our as-constructed PMH samples

are composed of 4 grains with random crystal orientations but identical size because X-ray analysis of lab-prepared PMHs of identical size but random crystallographic orientations.[20] When constructing PMHs, the Cartesian coordinates are expanded into Voronoi polyhedra with periodic boundary conditions (PBCs) to eliminate surface effects for mimicking large samples. Depending on *d*, MD samples of PMHs are generated with dimensions varying from around 9.1× 9.1× 9.1 to 18.1 × 18.1 × 18.1 nm^3.

Forcefield for PMHs

The monatomic water (mW) model is adopted to describe the interactions between water molecules,[36,37] in which each water molecule is coarse-grained as a single particle. The mW model is capable of forming tetrahedral HB structures by water molecules, and the interactions between water molecules is described by the Stillinger-Weber (SW) potential function. In the mW model, the guest methane molecule is also treated as a monatomic model represented by the SW two-body interaction. This mW forcefield can not only reproduce a range of properties of the liquid and solid phases of water and water-methane systems,[38-40] but also accurately describe the mechanical properties subjected to various loads.[24] Moreover, its computational efficiency is 2-3 orders of magnitude higher than that of the all-atom models.[37]

MD simulations

Prior to dynamic cyclic loads, as-generated PMHs undergo structural relaxations as follows. Initially, as-generated PMHs are structurally optimized to a local configuration with energy and force tolerances of 1.0×10^{-4} eV and 1.0×10^{-4} eV·$Å^{-1}$, respectively. Subsequently, as-optimized PMHs are further relaxed to alleviate unfavorable GB configurations with 10 ns at temperature of 270 K and confining pressure of P = 10 MPa under NPT (constant number of particles, constant pressure, and constant temperature) ensemble. T and P are regulated using Nosé-Hoover barostat and Nosé-Hoover thermostat with damping time constants of τ_T = 0.1 ps and τ_P = 1 ps, respectively. Following these MD relaxations, MD relaxations with another 10 ns are performed at T = 270 K under NVT (constant number of particles, constant volume, and constant temperature) ensemble, in which T is controlled using Nosé-Hoover thermostat with damping time of τ_T = 0.1ps. Finally, cyclic shear loads on as-relaxed PMHs are carried out to explore the dynamic mechanical behaviors. In the cyclic shear loads, a sinusoidal strain $\gamma(t) = \gamma_0 \sin(\omega t)$ with angular frequency of ω in the *x-y* direction is applied to PMHs using the deformation control technique, where γ_0 is represented by the largest shear strain amplitude assigned in the loads. Figure1A illustrates a schematic representation of PMHs subjected to shear strain. In this work, γ_0 = 8% is adopted to ensure that the system remains within the linear viscoelastic regime, where the dynamic moduli are independent of strain amplitude, while maintaining a sufficient signal-to-noise ratio in the stress response. The effects of ω and T on the dynamic mechanical responses of PMHs are examined. For example, when $\omega\tau_0 = 1.0 \times 10^{-3}$, T varies from 240 - 290 K, and $\omega\tau_0$ varies from 0.1 - 1.0×10^{-4} as T = 270 K. In the MD simulations of dynamic shear loading of PMHs, the particle motion follows the Newtonian equation with integration using the velocity-verlet algorithm with timestep of τ_0 = 2 fs. The atomic stress of each particle is computed according to the definition of *virial* stress.

Identification of polyhedral cages and water structure

Understanding the microstructural changes in PMHs subjected to cyclic shear loads is crucial to uncover the deformation mechanisms behind the viscoelastic properties. To accurately identify various microstructures such as polyhedral cages, the type of clathrate hydrate in PMHs, the Hierarchical Topological Ring (HTR) and HTR+ algorithms developed by Liu et al.[41] and Shi et al.[42] are utilized. The HTR algorithm identifies all types of intact polyhedral cages and distinguishes topological isomers that encapsulate multiple guest molecules.[41] Additionally, the HTR+ algorithm provides accurate identification of the type of crystalline clathrate hydrates such as sI, sII and sH hydrate phases, as well as structural transformations of clathrate cages.

RESULTS

Microstructural characteristics in PMHs

For conventional crystalline materials, *d*, the distribution of GBs, and their microstructures significantly influence dynamic mechanical behaviors of materials under load. In PMHs primarily composed of water molecules, these molecules form polyhedral cage structures by weak HBs. Figure 1B shows the variations in the number of conventional $5^{12}6^2$ and 5^{12} cages and unconventional $5^{12}6^3$, $5^{12}6^4$, $4^15^{12}6^2$ and $4^15^{12}6^3$ cages with the number of water molecules. However, conventional cages significantly outnumber unconventional cages, signifying sI type PMH samples. Specifically, the number ratio of $5^{12}6^2$-to-5^{12} cages is identified to be around 3:1, matching the proportion of $5^{12}6^2$ and 5^{12} cage in the unit-cell of sI hydrate. This linear dependence of cage number on water numbers and the consistent 3:1 ratio of $5^{12}6^2$-to-5^{12} cage confirm that *d* in PMH samples is proportionally controlled. Remarkably, the GBs in PMHs are primarily composed of unconventional clathrate cages, with the $4^15^{10}6^2$ cage being the most prevalent unconventional cages.[41,43,44]

Figures 1C&D illustrate the distribution profiles of potential energy of water molecules (E_w) within the $5^{12}6^2$ and 5^{12} cages in PMHs with varying *d*. For the 5^{12} cage, two prominent peaks are observed. The first peak corresponds to blue water molecules located on the pentagonal face of the $5^{12}6^2$ cage, shared with adjacent 5^{12} cage, displaying relatively lower E_w with approximately -0.552 eV. The second peak corresponds to the green water molecule located on the hexagonal faces of the $5^{12}6^2$ cage at angle of 150°, also shared with adjacent 5^{12} cage, with higher E_w (about -0.538 eV). Interestingly, for the $5^{12}6^2$ cages, a third peak appears at E_w = ~ -0.535 eV, relating to water molecules located on hexagonal faces at an angle of 60°. These results demonstrate that E_w depends on the specific position of the water molecule within the crystalline hydrate lattice. Furthermore, with increasing *d*, the distribution peaks corresponding to water molecules located inside the grains become more pronounced, reflecting the increasing dominance of conventional cages within the crystalline regions. These distribution profiles of E_w are dictated by the microstructures in PMHs, namely, PMHs with larger *d* correlate with a higher crystalline volume fraction and a lower GB volume fraction, potentially impacting overall structural stability and mechanical properties.

Figures 1E&F show the distribution profiles of E_w within the clathrate cages of 5^{12}, $5^{12}6^2$, $5^{12}6^3$, $5^{12}6^4$, $4^15^{10}6^2$ and $4^15^{10}6^3$ for PMHs with d = 8 and 14 nm, respectively, while the cases for d = 11 and 17 nm are shown in Figure S1. Comparison reveals sharper peaks in the distribution profiles of E_w within conventional 5^{12} and $5^{12}6^2$ cages for PMHs with larger *d* than those with smaller *d*. This difference arises because smaller *d* lead to a larger contact area between grains and GBs, resulting in a higher proportion of water molecules located at these interfacial regions. Note that the thickness of GBs in PMHs is independent on *d*. In contrast, for unconventional $5^{12}6^3$, $5^{12}6^4$, $4^15^{10}6^2$ and $4^15^{10}6^3$ cages within GB regions, the distribution profiles of E_w are broader, with less distinct peaks.[24,25,44,45] Moreover, these distribution curves of E_w show no dependence on *d*. Water molecules within unconventional cages consistently exhibit higher E_w than those within conventional cages. E_w rendering maps confirm that water molecules with high E_w in unconventional cage are primarily distributed at GBs and at the surface of grains contacting GBs.[24,25,44,45] Among unconventional cages, water molecules in $4^15^{10}6^2$ cages show a lower E_w distribution than those in other unconventional cages, explaining the higher prevalence of $4^15^{10}6^2$ cages within GB regions.

Mechanical loss and energy dissipation in PMHs

Figure 2A shows the typical cyclic shear stress σ (blue balls) responses of a PMH with d = 14 nm subjected to a sinusoidal shear strain $\gamma(t) = \gamma_0 \sin(\omega t)$ (red balls and red line), as well as the sinusoidal function fitting of cyclic σ (blue line). The cyclic σ and cyclic strain γ are out-of-phase, characterized by a lag between the cyclic σ and cyclic γ, namely, where δ is the phase shift between the cyclic σ and the cyclic γ. This phase shift is evident in the sinusoidal fitting of the stress data by $\sigma(t) = \sigma_0 \sin(\omega t + \delta)$ in Figure 2A.

Figure 2B displays the resultant σ curves for PMHs with d = 14 nm at T = 270 K subjected to $\omega\tau_0 = 2.0 \times 10^{-2}$, 1.0×10^{-2}, 2.0×10^{-3}, 1.0×10^{-3}, 2.0×10^{-4} and 1.0×10^{-4}, while Figure 2C shows the resultant σ curves for PMHs with d = 14 nm subjected to $\omega\tau_0 = 1.0 \times 10^{-3}$ at T = 240, 250, 260, 270, 280 and 290 K. Results for PMHs with other d are presented in Figure S2. Both increasing T and decreasing ω cause a clear reduction in the maximum cyclic σ_0 and an increase in the phase shift δ. Figure 2D plots σ_0 against ω for PMHs with d = 8 - 17 nm at T = 270 K, demonstrating a strong *d*-dependence of σ_0. At a given ω, PMHs with smaller *d* exhibit higher σ_0. Moreover,

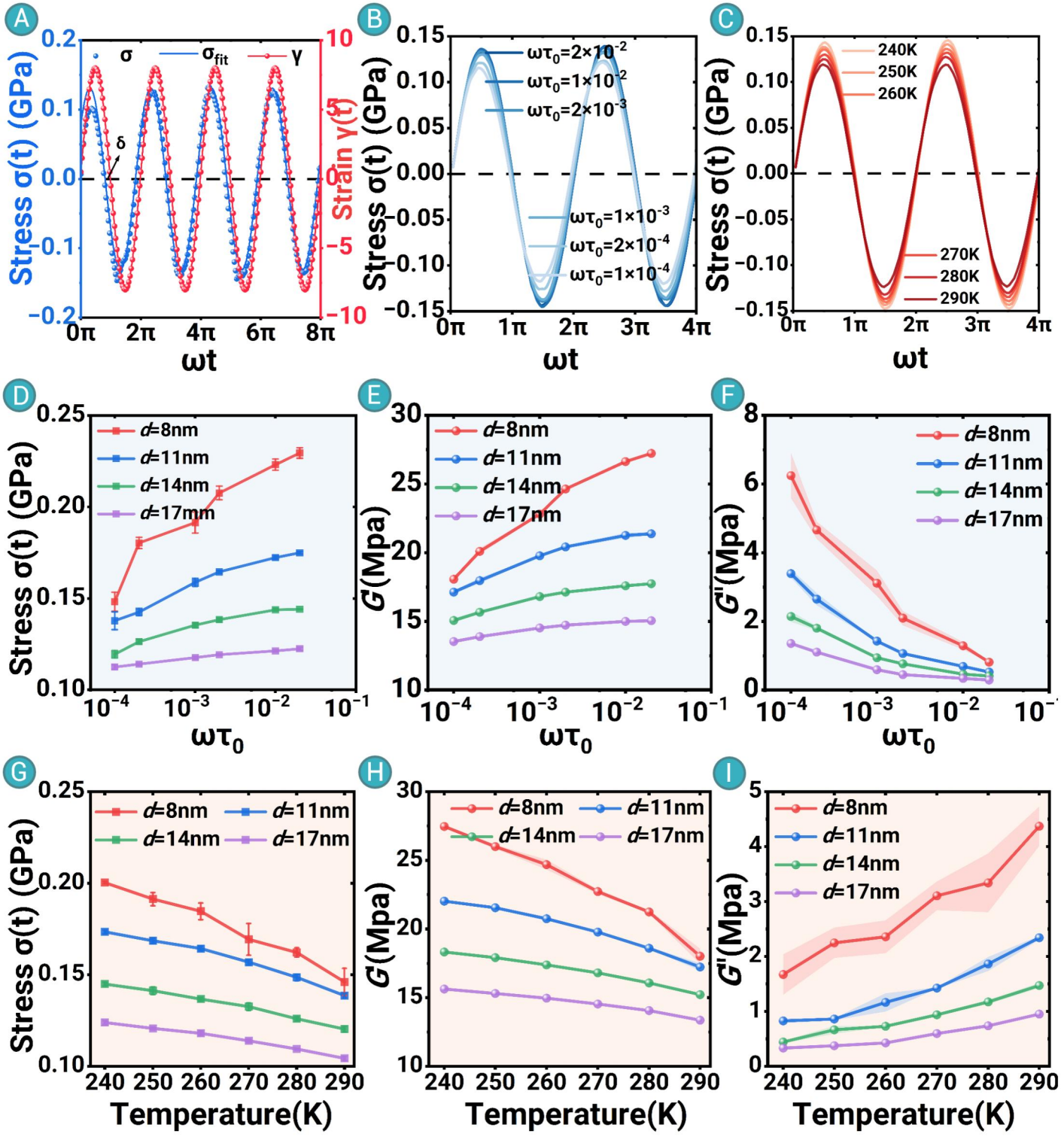

Figure 2. Dynamic mechanical properties of polycrystalline methane hydrates (PMHs) (A) Typical cyclic shear stress σ and shear strain γ relationship in PMHs, illustrating the viscoelastic response of PMHs under oscillatory loading. (B) Cyclic shear stress σ responses of PMHs with d = 14 nm under frequencies ranging from 1×10^{-4} to 2×10^{-2}, showing the frequency-dependent variation in stress amplitude. (C) Cyclic shear stress σ responses of PMHs with d = 14 nm at T ranging from 240 to 290 K, highlighting the temperature sensitivity of the mechanical response. (D)-(F), σ_0, G' and G'' of PMHs plotted against $\omega\tau_0$ (1×10^{-4} to 2×10^{-2}) for grain sizes d = 8, 11, 14, and 17 nm at T = 270 K, demonstrating the combined effects of loading frequency and grain size on elastic and viscous behavior. (G)-(H), Temperature-dependent σ_0, G' and G'' of PMHs with grain sizes d = 8, 11, 14, and 17 nm, obtained at $\omega\tau_0 = 1\times10^{-3}$ over the temperature range of 240–290 K, revealing the evolution of viscoelastic properties with temperature.

PMHs with smaller d show stronger sensitivity of σ_0 to change in ω. Increasing ω causes a more pronounced enhancement in σ_0 in PMHs with small d.

To quantitatively characterize the dynamic mechanical properties of PMHs, the complex modulus is introduced as follows

$$G^*(\omega) = G'(\omega) + iG''(\omega)$$

with

$$G' = \frac{\sigma_0}{\gamma_0}\cos\delta$$

$$G''=\frac{\sigma_0}{\gamma_0}\sin\delta$$

where the real part of the complex modulus G' is defined as the storage modulus that characterizes the elastic properties of PMHs, while the imaginary part of the complex modulus G'' is defined as the loss modulus, characterizing energy dissipation of PMHs.

Figures 2E&F show the response of G' and G'' of PMHs with d = 8 - 17 nm to ω at T = 270 K. Increasing ω causes G' to rise and G'' to fall. The rate of increase in $G'$and decrease in G'' diminishes at higher ω. Under high ω, shear straining suppresses structural relaxation within the PMHs, minimizing the mechanical strength difference between crystalline grains and GBs. Consequently, G' significantly exceeds G'' at high ω, and PMHs exhibits primarily elastic deformation. Conversely, decreasing ω promotes structural relaxation of PMHs, including diffusion, GB sliding, and structural transformations, resulting in significant energy dissipation. At lower ω, G'' approaches G' and changes rapidly with ω, resulting in viscoelastic deformation.[33]

Figure 2G shows the variations of σ_0 with T for PMHs with d = 8 - 17 nm at $\omega\tau_0 = 1.0 \times 10^{-3}$. As T increases, σ_0 decrease more sharply. PMHs with d = 8 nm shows stronger sensitivity of σ_0 to T, showing a more pronounced reduction in σ_0 with increasing T. This arises because PMHs with smaller d possess higher volume fractions of metastable GB structures. Figures 2H&I display the responses of G' and G'' of PMHs at $\omega\tau_0 = 1.0 \times 10^{-3}$ to T, respectively. As T increases, G'' of PMHs increases, while G' of PMHs decreases. Both G' and G'' exhibit nonlinear relationships with T, similar to their behavior with ω. Comparison of the ω and T spectra of G' and G'' indicates that, similar to viscoelastic polymers, time and T have a synergistic effect on the dynamic mechanical behaviors of PMHs, following the time-temperature superposition principle.[46-49] Increasing T has an effect equivalent to decreasing ω on deformation of PMHs. This implies that for sediment-hosted PMHs, increasing T or decreasing ω equivalently impacts rheological behavior.

The ratio of G''-to-G' is the tangent of δ, known as the loss tangent (tan δ), which characterizes the magnitude of mechanical loss. Figure 3A shows tan δ versus d for different $\omega\tau_0$ values at 270 K. For each ω, tan δ exhibits a nonlinear relationship with d. PMHs with smaller d or subjected to lower ω yield higher tan δ. This indicates that for a given T, as d and ω decrease, PMHs dissipate more energy under cyclic shear loads, causing PMHs to transition from elastic to viscoelastic behavior with significant mechanical loss. Here, we next focus on the dependencies of G' and G''on d. Figure 3B&C shows the relationships between G' and G'' of PMHs and d under $\omega\tau_0 = 1.0 \times 10^{-2}$, 1.0×10^{-3}, 1.0×10^{-4}, respectively. Both G' and G'' of PMHs vary nonlinearly with d, describable by exponential functions. With increasing d, reductions in both G' and G'' become less pronounced. Moreover, the nonlinear changes in G' and G'' with d differ. At low $\omega\tau_0$, the reduction in G' with d is less pronounced, while the opposite trend is observed for G''. This indicates that PMHs with different d show distinct responses of dynamic moduli to $\omega\tau_0$. PMHs with smaller d subjected to low $\omega\tau_0$ readily transition from elastic to viscoelastic behavior, suggesting that sediments-hosted NGHs with small d show reduced mechanical resistance to dynamic disturbances. Consequently, geo-mechanical properties of seabed containing small-grained NGHs are easily weakened under dynamic force due to large mechanical loss reducing cementation.

Figure 3D illustrates the relationship between tan δ and d for PMHs at different T but constant $\omega\tau_0 = 1.0 \times 10^{-3}$. At different T, PMHs show nonlinear changes in tan δ with d. PMHs with smaller d or at higher T yield higher tan δ. This indicates that PMHs with smaller d or at higher T dissipate more energy under cyclic shear, making them more prone to viscoelastic deformation with greater mechanical loss. Figures 3E&F show the relationships between G' and G'' of PMHs and d at T = 240, 270 and 290 K, respectively. Similar to the results upon different $\omega\tau_0$, both G' and G'' change nonlinearly with d. At a given T, PMHs with larger d yield smaller G' and G''. The reduction in G' with d becomes less significant with increasing T, whereas for G'', opposite reduction is found. This demonstrates that PMHs with different d demonstrate different dynamics moduli in response to T. PMHs with smaller d or at higher T more readily transition from elastic to viscoelastic behavior, indicating that NGHs with small d in sediments tend to undergo mechanical loss under disturbances at elevated T. Thus, seabed containing small-grained NGHs are more easily destabilized by mechanical disturbances at higher T.

To further elucidate the unique relationship between G'', $\omega\tau_0$ and d for PMHs, the Cross model[50-52] for non-Newtonian fluids is adopted as follows

$$G''=\eta_\infty+\frac{\eta_0-\eta_\infty}{1+(k*\omega\tau_0)^n}$$

where η_0 and η_∞ are the loss moduli at the low- and high-ω limits, respectively. k is the "characteristic" time scale, related to the relaxation time of a material. n is the flow behavior index or non-Newtonian index. The fitted Cross-model parameters (η_0, η_∞, k, and n) are summarized in Table S1 in the Supporting Information.

Figure 3G compares MD results for G'' against $\omega\tau_0$ for PMHs with d = 11, 14 and 17 nm against fits using the Cross-model. The model accurately describes the nonlinear relationships between G'' and $\omega\tau_0$. This indicates that PMHs exhibit non-Newtonian fluid properties, transitioning from elastic to viscoelastic behavior with decreasing ω. Figures 3I&J show the changes of the characteristic parameters η_0, η_∞, k, and n with d, respectively. Both η_0 and η_∞ monotonically reduce with increasing d. PMHs with larger d yield smaller elastic viscoelastic limits, indicating poorer inherent elastic properties and reduced susceptibility to viscoelastic behavior. With increasing d, k decreases, implying that smaller-grained PMHs require longer relaxation time to accommodate cyclic γ, resulting in larger energy dissipation. Conversely, n increases with increasing d, signifying that larger-grained PMHs exhibit better elastic performance and resist energy dissipation under cyclic shear. In a nutshell, the microstructure of PMHs is a key factor governing their dynamic mechanical behaviors.

Dissipation mechanisms in PMHs

The G' and G'' spectra reveal that dissipation in PMHs subjected to cyclic shearing loads exhibits monotonic change across a broad range of $\omega\tau_0$ and T, lacking significant GB internal friction peaks, which is characteristic of a 'high-temperature background (HTB)' dissipation mechanism.[53] Similar observations have been reported in ceramics and geological materials, particularly concerning high-T viscoelastic relaxation in polycrystals.[54-57] For instance, melt-free and basaltic (complex alumino-silicate) materials exhibit only HTB dissipation linked to transient diffusion creep. Similarly, dense, high-purity polycrystalline MgO show monotonically ω- and T-dependent dissipation without superimposed peaks. This phenomenon is primarily attributed to the suppression of elastically accommodated GB sliding.[58] GB sliding, diffusion, and structural transformations are critical mechanisms for internal dissipation in polycrystalline materials.[30,59] To elucidate the dissipation mechanisms of PMHs subjected to cyclic shearing, molecular diffusion and microstructural evolution in PMHs are in-depth investigated at the molecular level.

Diffusion heterogeneity across microstructures. Figures 4A&B illustrate the mean square displacements (MSD) of water and methane molecules in PMHs with d = 8 and 14 nm subjected to cyclic loading at $\omega\tau_0 = 1.0 \times 10^{-2}$, 1.0×10^{-3}, and 1.0×10^{-4}, respectively. The MSD is defined as $\langle|r_i(t)-r_i(0)|^2\rangle$, where $r_i(t)$ and $r_i(0)$ denote the positions of particle i at time t and the reference time, respectively. Methane molecules exhibit significantly larger MSD values than water molecules. PMHs with smaller d yield higher MSD for species due to their larger fraction of metastable GBs structures, leading to greater energy dissipation. This explains the higher tan δ in PMHs with smaller d. For PMH with a given d subjected to lower $\omega\tau_0$, larger MSD values are observed, consistent with higher tan δ of PMHs subjected to lower $\omega\tau_0$.

Diffusion coefficients (D) for water and methane molecules in PMHs subjected to cyclic shearing loads are computed from the MSD curves. Figures 4C&S3A show the changes in D for water and methane molecules with d at different $\omega\tau_0$. For each $\omega\tau_0$, PMHs exhibit nonlinear relationship between D and d. Similar to the previously observed nonlinear relationship between $G''$and d, the nonlinear relationship between D and d is well-described by exponential functions. As d decreases, D for both methane and water molecules increase, attributable to the higher proportion of metastable GBs where molecules exist in a disordered, non-perfect crystalline states. In addition, as $\omega\tau_0$ decreases, D for methane and water molecules also decrease. This occurs because cages at GBs experience weaker mechanical perturbation at low $\omega\tau_0$, enabling structural transformations between

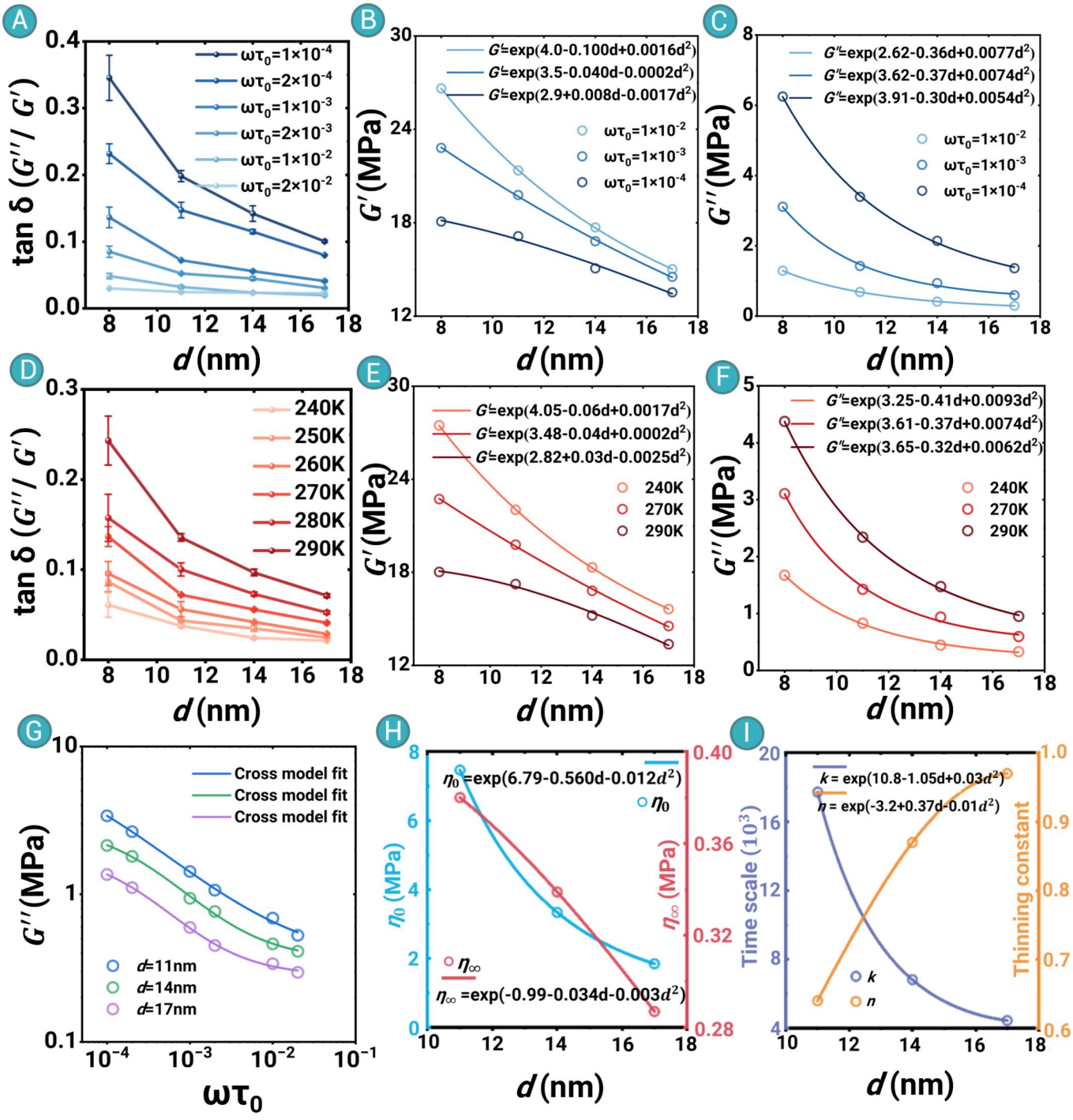

Figure 3. Relationship between dynamic moduli and *d* in PMHs (A) Variation of the loss tangent (tan δ) with d (8, 11, 14, and 17 nm) at T = 270 K under normalized frequencies ranging from $\omega\tau_0$ =1 × 10^{-4} to 2 × 10^{-2}, where each curve corresponds to a specific frequency, reflecting the coupled dependence of the viscoelastic response on both grain size and loading frequency. (B)-(C) Grain-size dependence of G' and G'' at T = 270 K under different $\omega\tau_0$ (1 × 10^{-2}, 1 × 10^{-3}, and 1 × 10^{-4}), demonstrating the effects of grain size and frequency on the viscous-elastic response. (D) Variation of tan δ with d (8-17 nm) at $\omega\tau_0$ = 1.0 × 10^{-3} over a temperature range of 240-290 K, highlighting the influence of grain size and temperature on the viscoelastic balance. (E)-(F) The relationship between G' and G'' with d at $\omega\tau_0$ = 1.0 × 10^{-3} under different temperatures (T = 240, 270, and 290 K), demonstrating the combined effects of temperature and grain size on elastic stiffness and viscous response. (G) Frequency dependence of G'' fitted using Cross model over the range $\omega\tau_0$ = 1 × 10^{-4} to 2 × 10^{-2} for d = 11, 14, and 17 nm, capturing the non-Newtonian viscoelastic behavior. (H)-(I), Cross model parameters (η_0, η_∞, k, and n) as a function of d, characterizing the evolution of rheological properties with microstructural scale.

clathrate cages, which lowers D.

Figures 4D&E show the MSD of water and methane molecules in PMHs with d = 8 and 14 nm under cyclic loading at $\omega\tau_0$ = 1.0×10^{-3} and T = 240, 270 and 290 K. At a given T, PMHs with smaller d show larger MSDs, indicating higher energy dissipation and explaining their increased tan δ. For a fixed d, PMHs at higher T yield larger MSD values, consistent with the higher tan δ of PMHs at elevated T. Figures 4F&S3B illustrate the changes in D of water and methane molecules with d at different T, respectively. Nonlinear relationships between D and d are again observed and well-fitted by exponential function. As d decreases, D of methane and water increases nonlinearly. Additionally, as T rises, D of methane and water molecules also increase, and D shows greater sensitive to T than to changes in $\omega\tau_0$. This heightened sensitivity arises because molecular motion within GBs intensifies at higher T.

Figures 4G&H provide localized snapshots of PMH with d = 8 and 14 nm at

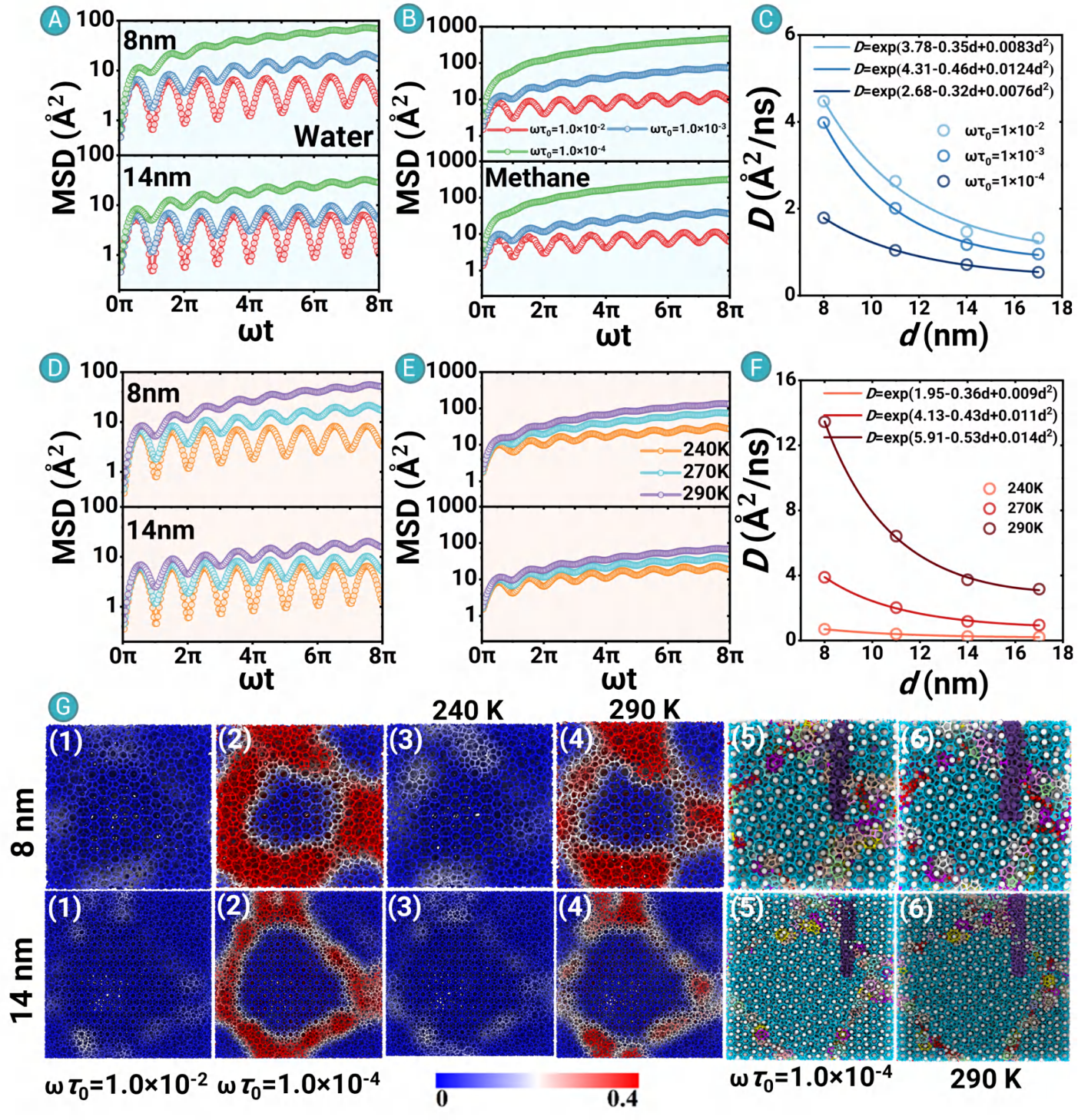

Figure 4. Molecular diffusions in polycrystalline methane hydrates (A) The MSD values of water and (B) methane particles in PMHs with d = 8 and 14 nm subjected to frequencies $\omega\tau_0$ = 1 × 10^{-2}, 1 × 10^{-3}, and 1 × 10^{-4} (T= 270 K). (C) Corresponding diffusion coefficients of water and methane as a function of grain size *d* at the three frequencies, illustrating the frequency-dependent mobility enhancement. (D) MSD of water and (E) methane molecules in PMHs with *d* = 8 nm and 14 nm at temperatures T = 240, 270, and 290 K ($\omega\tau_0$ = 1.0 × 10^{-3}). (F) Diffusion coefficients of water and methane as a function of *d* at the three temperatures, showing the thermally activated nature of diffusion. (G) and (H), Cross-sectional snapshots of PMHs with *d* = 8 nm and 14 nm subjected to $\omega\tau_0$ =1.0 × 10^{-2} and 1.0 × 10^{-4}, *T* = 240 and 270 K, $\omega\tau_0$ =1.0 × 10^{-4} and *T* = 290 K. Water particles in snapshots of 1-4 are rendered according to their normalized offsets of displacement vectors (shear strain); 5, 6 are rendered according to the type of cages they belong.

$\omega\tau_0$ = 1.0 × 10^{-2} and 1.0 × 10^{-4}, *T* = 240 and 290 K, $\omega\tau_0$ = 1.0 × 10^{-4} and *T* = 290 K, respectively. In Figures 4G(1-4) and H(1-4), water molecules are colored based on their normalized offsets of displacement vectors (shear strain) for clarification, whereas in Figures 4G(5, 6) & H(5, 6), the color scheme indicate type of clathrate cage, with selected water molecules mint green-highlighted to visualize potential GB sliding. Water molecule diffusion is unevenly distributed, being more pronounced near GBs. PMHs with *d* = 8 and 14 nm exhibit enhanced local diffusion in the vicinity of GBs at lower ω or higher *T*. At *T* = 240 K, the diffusion pattern resembles that at high $\omega\tau_0$ = 1.0 × 10^{-2}, while at *T* = 290 K, the pattern resembles that at low $\omega\tau_0$ = 1.0 × 10^{-4}, demonstrating time-temperature equivalence in PMHs under cyclic shear. Comparing Figure 4G(5) with Figure 4H(5) reveals that PMHs with smaller *d* have a higher proportion of water diffusion at GBs, contributing to larger energy dissipation. Additionally, methane molecules at GBs can diffuse into the crystalline cages and displace existing methane molecules, facilitating exchanges of guest methane molecules. Significant GB sliding is absent,

supporting the concept of its inhibition by elastic accommodation. However, from Figures 4G(6) and H(6), slight GB sliding is observed in PMH with d = 8 nm at T = 290 K. As T increases, the thermal motion of molecules at GBs intensifies, enhancing diffusion and weakening elastic accommodation that inhibits GBs sliding. The larger proportion of GBs in PMH with d = 8 nm allows both GB sliding and diffusion to occur concurrently.

Cage transformation pathways in PMHs. Unlike conventional polycrystalline materials, PMHs consist primarily of water molecules, forming clathrate cages through HBs. The insertion, removal, and rotation of water molecules within the cages drive structural transformations, including cage interconversions and dissociation/reformation processes, particularly within GBs region rich in unconventional metastable cages.[60] Subjected to external loads, these transformations in metastable cages at GBs constitute a significant energy dissipation pathway.

Figure 5A illustrates the roadmap of structural transformation pathways along 20 identified types of clathrate cages in PMHs subjected to cyclic shearing, in which color-coded by the number of transformation pathways by which a cage transforms to or be transformed from another cage. The 5^{12}, $5^{12}6^2$, $5^{12}6^3$, $5^{12}6^4$, $4^15^{10}6^2$, and $4^15^{10}6^3$ cages exhibit the highest frequency of occurrence and the most transformation pathways, indicating their dominant role in structural transformations to cyclic shear. Cage transformations serve as a primary mechanism for releasing shear strain energy in PMHs, distinct from conventional polycrystals such as metallic, semi-conducting materials where dislocation motion predominates.[61-63]

Figure 5B illustrates the unique transformation pathways of $5^{12}6^2$-5^{12}, $5^{12}6^2$-$4^15^{10}6^2$, $4^15^{10}6^2$-5^{12}, and $4^15^{10}6^2$-$5^{12}6^2$ cages that are frequently-identified in PMHs subjected to cyclic shear. A conventional $5^{12}6^2$ cage transforms into unconventional $4^15^{10}6^2$ cage by removing water molecules from two five-membered rings. Conversely, $4^15^{10}6^2$ cage reverts to $5^{12}6^2$ cage by removing water molecules between four- and five-membered rings and inserting others. As a result, cage transformations of $5^{12}6^2 \leftrightarrow 4^15^{10}6^2$ occur during the cyclic shear loads. Similarly, both $5^{12}6^2$ and $4^15^{10}6^2$ cages convert to 5^{12} cage via removal/insertion mechanisms. All 20 cage types undergo diverse interconversions through water molecule rearrangement.

Figure 5C quantifies transformation frequencies for the six prevalent cages of 5^{12}, $5^{12}6^2$, $5^{12}6^3$, $5^{12}6^4$, $4^15^{10}6^2$, and $4^15^{10}6^3$ in PMH with d = 14 nm subjected to $\omega\tau_0$ from 2.0 × 10^{-2} - 1.0 × 10^{-4} and T from 240 - 290 K. PMHs under high T or low $\omega\tau_0$ display enhanced counts of cage transformations. In terms of the number of cage transformations, the $4^15^{10}6^2$ cage shows the highest cage transformation activity, while the $5^{12}6^4$ cage shows the least. This aligns with E_w observations. The $4^15^{10}6^2$ cage has the lowest E_w among unconventional cages, and $5^{12}6^4$ cage demonstrates the highest E_w, indicating a preference for transitions toward lower-energy cage configurations.

Figure 5D shows the largest percentages of other five cages transformed into frequently-observed 5^{12}, $5^{12}6^2$, $5^{12}6^3$, $5^{12}6^4$, $4^15^{10}6^2$, or $4^15^{10}6^3$ in PMHs subjected to $\omega\tau_0$ = 1.0 × 10^{-4}. 5^{12}, $5^{12}6^2$, $4^15^{10}6^3$, $4^25^86^2$ and $4^25^86^4$ cages show the largest percentages to transform into $4^15^{10}6^2$ cage, and they are sorted as 5^{12} > $5^{12}6^2$ > $4^15^{10}6^3$ > $4^25^86^2$ > $4^25^86^4$ cage in terms of the magnitude of percentage. Whereas for 5^{12}, $5^{12}6^2$, $5^{12}6^3$, $5^{12}6^4$ and $4^15^{10}6^3$ cages, their five main cage precursors, in descending order, are $4^15^{10}6^2$, $4^25^86^1$, $4^25^86^2$, $4^15^{10}6^3$ and 4^35^9 cages, and $4^15^{10}6^2$, $4^15^{10}6^4$, $4^15^{10}6^3$, $4^25^86^3$ and $5^{12}6^3$ cages, and $4^15^{10}6^4$, $5^{12}6^2$, $4^15^{10}6^3$, $4^15^{10}6^5$, and $5^{12}6^4$ cages, and $4^15^{10}6^3$, $5^{12}6^3$, $4^15^{10}6^4$, $5^{12}6^5$, and $5^{12}6^2$ cages, and $4^15^{10}6^2$, $5^{12}6^2$, $5^{12}6^3$, $4^15^{12}6^4$, and 5^{12} cages, respectively. Interestingly, among the cages discussed above, the $4^15^{10}6^2$ cage acts as a central transformation hub: it is both the most frequent product of cage transformations and the cage with the highest probability of converting into other types, underscoring its pivotal role in the microstructural evolution of polycrystalline methane hydrates under shear.

Figure S4 shows the variations in the transformation rate of 5^{12}, $5^{12}6^2$, $5^{12}6^3$, $5^{12}6^4$, $4^15^{10}6^2$, and $4^15^{10}6^3$ cages (R) which is defined as the ratio of the number of transformation-to the number of water molecules in PMHs with d. PMHs subjected to different $\omega\tau_0$ and different T yield nonlinear relationships between R and d. Subjected to a given $\omega\tau_0$ and T, PMHs with smaller d possess higher R due to larger metastable GB fractions, enhancing energy dissipation. At a given d, PMHs subjected to lower $\omega\tau_0$ and higher T present higher R, reflecting longer structural transformation timescales at lower $\omega\tau_0$ or thermally activated processes. Figure S5 specifically present the variation in R of $5^{12}6^2$ and $4^15^{10}6^2$ with d, mirroring the nonlinear trends of G'' and D. At a given $\omega\tau_0$, PMHs with smaller d yield larger R. In addition, with increasing d, reduction in R becomes less pronounced. At a given T, PMHs with smaller d exhibit larger R, and reduction in R is also less significant with increasing d. PMHs with larger d yield lower volume proportion of GBs, resulting in lower R of GBs and grain cages, which further proves that PMHs with larger d are less likely to undergo viscoelastic deformation.

GB-dominated phase transition behavior. Polycrystalline structures can undergo dynamic recrystallizations and phase transformations under changes in temperature/stress, contributing to internal friction.[64,65] Phase transformation is one of the mechanisms behind internal frictions in polycrystalline materials. Experiments and first-principle calculations revealed that methane hydrates undergo pressure-induced phase transformations,[12,66-71] marking structural analysis key to understanding PMH dissipation. Figures 6A&B show the variations in the percentage of sI/sII phase hydrates in PMHs with d = 8 and 14 nm at T = 270 K subjected to $\omega\tau_0$ = 1.0 × 10^{-2}, 1.0 × 10^{-3} and 1.0 × 10^{-4}, respectively. Due to the large difference in the fractions of sI and sII structures, a broken y-axis is used to better visualize the variation of the less abundant sII phase. Local fluctuations in the percentage of sI and sII phase hydrate in PMHs during the cyclic shearing indicates dynamic sI ↔ sII phase transitions mediated by cage transformations. Intriguingly, such sII → sI phase transitions in methane hydrates and mixed gas hydrates (methane with small amounts of ethane and propane) under pressure conditions at wide range T were confirmed via experimental techniques such as time-resolved in-situ neutron diffraction and Raman spectroscopy,[71,72] while the sI→ sII phase transitions in sI methane hydrate remain unobserved. Lower $\omega\tau_0$ causes stronger fluctuations and a pronounced increase in the percentage of sI and sII phase hydrate in PMHs, indicating enhanced dynamic sI ↔ sII phase transitions. In addition, with decreasing $\omega\tau_0$, the percentage of sII phase hydrate increases more pronouncedly, whereas for sI phase hydrate, opposite behavior is detected. This signifies that PMHs under lower $\omega\tau_0$ demonstrate more remarkable sI → sII phase transition than sII → sI one.

Figure 6C quantifies the number of seven types of cages involved in sI ↔ sII phase transitions, including 5^{12}, $5^{12}6^2$, $5^{12}6^3$, $5^{12}6^4$, $4^15^{10}6^2$, $4^15^{10}6^3$ and $4^15^{10}6^4$ in PMHs with d = 8 nm at 270 K subjected to $\omega\tau_0$ = 1.0 × 10^{-2}, 1.0 × 10^{-3} and 1.0 × 10^{-4}, as well as shear-free condition. Here, the shear-free condition represents the initial equilibrium state of PMHs before the application of cyclic shear. Compared to shear-free condition, PMHs subjected to high $\omega\tau_0$ exhibit reduced number of each type of cages. At $\omega\tau_0$ = 1.0 × 10^{-4}, however, increase in the number of 5^{12} and $5^{12}6^4$ cages which form sII hydrate, is observed. Moreover, the number of $5^{12}6^3$ cage increases, while the number of $5^{12}6^2$ cage that is one of component of sI hydrate decreases. These number changes of cages indicate that phase transition from sI → sII occurs in PMHs subjected to $\omega\tau_0$ = 1.0 × 10^{-4}. Figures 6G(1)&(2) show perspective snapshots of PMH with d = 8 nm subjected to $\omega\tau_0$ = 1.0 × 10^{-2} and 1.0 × 10^{-4}, respectively. As is indicated by the arrows, structural transition from sI → sII hydrate in PMH subjected to $\omega\tau_0$ = 1.0 × 10^{-4} is vividly illustrated. Furthermore, the regions where sII hydrate exists indicate that the sI ↔ sII transformations observed here originate from local and transient cage conversions within GB regions and defective structures, and do not represent a bulk thermodynamic phase transition of the hydrate lattice.

Figures D&E show the variations in the percentage of sI and sII phase hydrates in PMHs with d = 8 and 14 nm subjected to $\omega\tau_0$ = 1.0 × 10^{-3} at T = 240, 270 and 290 K, respectively. PMH with d = 8 nm shows greater sensitivity to changes in T, and with the increase of T, sII phase hydrate decreases significantly compared to shear-free condition, while sI phase hydrate remains in dynamic equilibrium. For PMHs with d = 14 nm, compared to shear-free condition, both sI and sII phase hydrates tend to decrease as T increases, though the overall reduction is insignificant. This indicates that T primarily affects the changes in the sI and sII hydrate phases at GBs. Since PMHs with smaller d have larger proportion of GBs, they are more sensitive to changes in T. As T rises, the metastable GB structures are more likely to dissociate, leading to reduction in solid-state hydrates in PMHs.

Figure 6F displays the number of 5^{12}, $5^{12}6^2$, $5^{12}6^3$, $5^{12}6^4$, $4^15^{10}6^2$, and $4^15^{10}6^3$ cages in PMHs with d = 8 nm subjected to $\omega\tau_0$ = 1.0 × 10^{-3} at T = 240 - 290 K, as well as loading-free conditions. Compared to shearing-free cases,

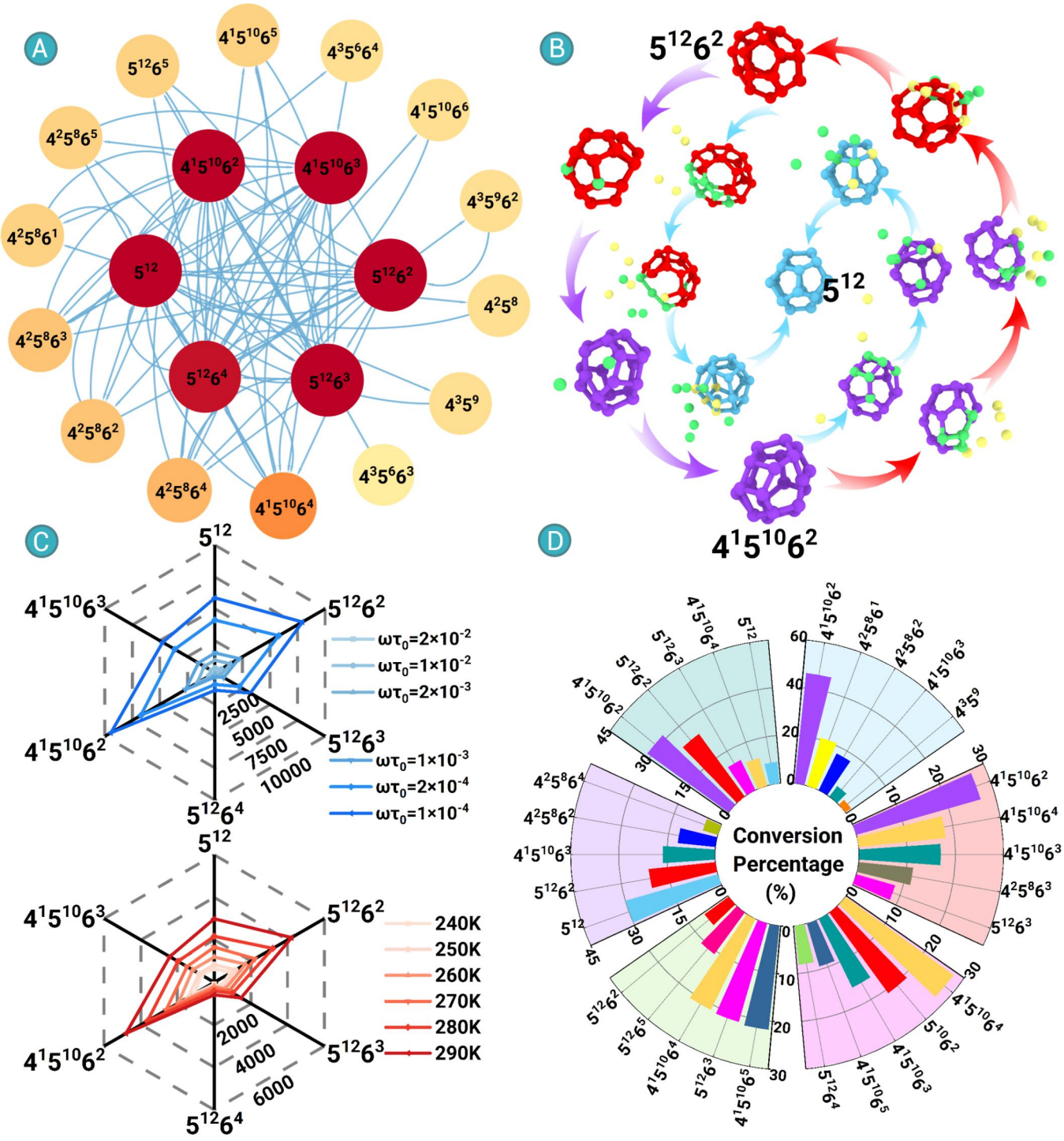

Figure 5. Structure transformations between clathrate cages in polycrystalline methane hydrates (A) Cage transformations identified in PMHs. (B) Structural transformations of the most frequently-observed 5^{12}, $5^{12}6^2$, $5^{12}6^3$, $5^{12}6^4$, $4^15^{10}6^2$, and $4^15^{10}6^3$ cages in PMH with d = 14 nm, for example, cage transformations of $5^{12}6^2 \rightarrow 4^15^{10}6^6$, $4^15^{10}6^2 \rightarrow 5^{12}6^2$, $5^26^2 \rightarrow 5^{12}$, $4^15^{10}6^2 \rightarrow 5^{12}$. (C) The number of structural transformations for the most frequently-observed 5^{12}, $5^{12}6^2$, $5^{12}6^3$, $5^{12}6^4$, $4^15^{10}6^2$, and $4^15^{10}6^3$ cages in PMH with d = 14 nm subjected to $\omega\tau_0$ from 2.0×10^{-2} - 1.0×10^{-4} and T from 240 - 290 K. (D) The percentage of other cages transformed into the most frequently-observed 5^{12}, $5^{12}6^2$, $5^{12}6^3$, $5^{12}6^4$, $4^15^{10}6^2$, and $4^15^{10}6^3$ cages in PMHs subjected to $\omega\tau_0 = 1.0 \times 10^{-4}$. 5^{12}, $5^{12}6^2$, $5^{12}6^3$, $5^{12}6^4$, $4^15^{10}6^2$, and $4^15^{10}6^3$ cages are indicated by the blue, the red, the pink, the green, the purple and the cyan sectors, respectively.

PMHs show smaller number of those cages, with much more reduction at higher T. This indicates that both sI and sII phase hydrates decrease as T increases. Figures 6G(3)&(4) show snapshots of PMHs with d = 14 nm at T = 240 and 290 K, respectively. It is demonstrated significant reduction in sI and sII phases at high T. At low ω and high T conditions, the reduction of sI phase hydrates and the increase of sII phase or GBs are dynamic, which is one of the main reasons for the decrease in G' and the increase in G'' of PMHs under cyclic shear, producing the transition of the mechanical behavior of PMHs from elastic to viscoelastic.

Transcrystalline fracture formation

Subjected to high ω, structures of PMHs possess short-time relaxations. As a result, diffusion, GB sliding, cage transformations, and phase transformations are largely suppressed in response to high $\omega\tau_0$, leading to high σ_0. When σ_0 exceeds the strength limit, PMH undergoes plastic deformation via dissociation of cages in response to cyclic shear, causing mechanical loss.

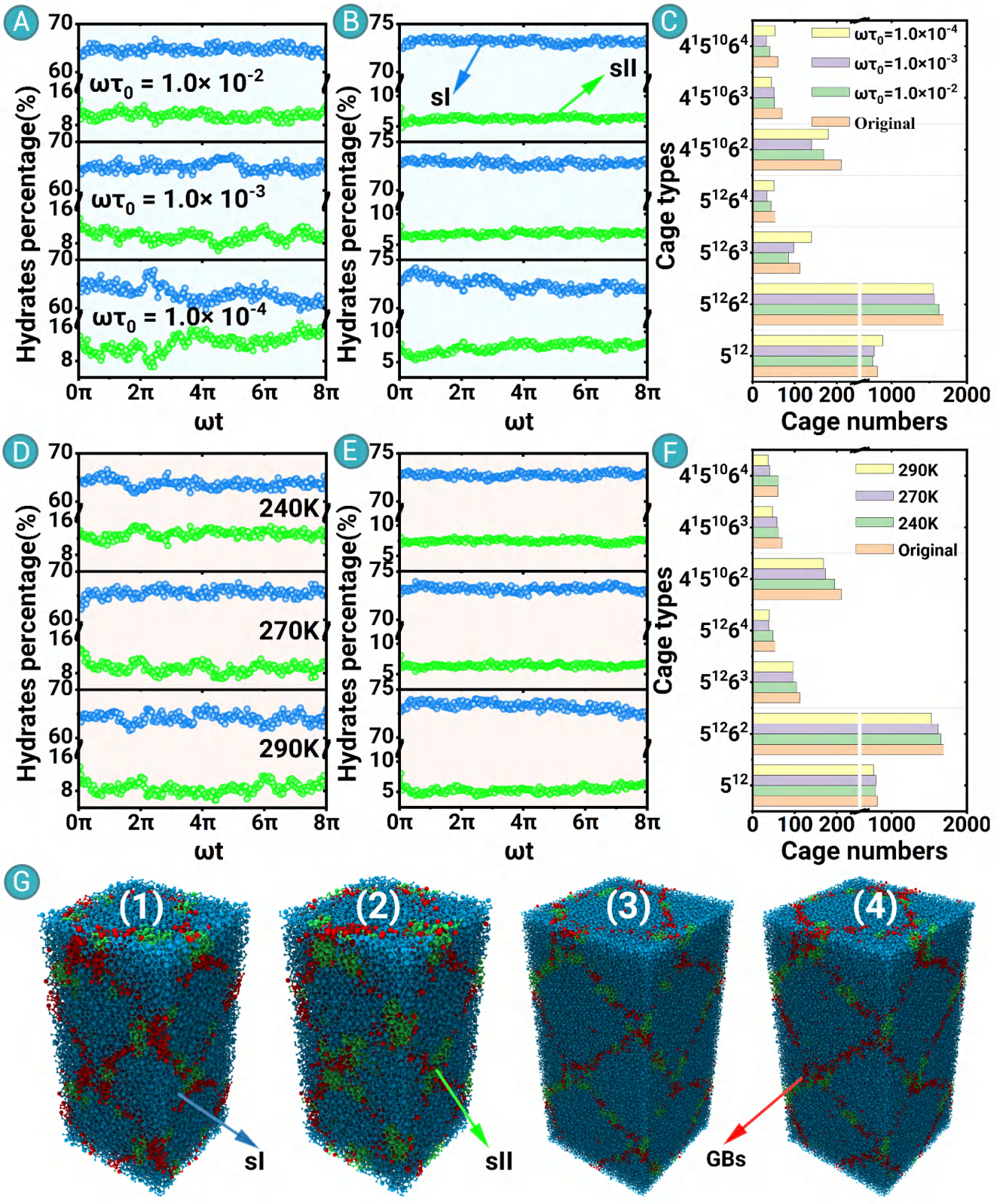

Figure 6. Microstructure changes in polycrystalline methane hydrates subjected to cyclic shear loads (A) and (B) Changes in the percentage of sI and sII phase hydrates in PMHs with d = 8 and 14 nm subjected to $\omega\tau_0$ = 1.0× 10^{-2} -1.0 × 10^{-4} at T = 270 K. (C) The number of 5^{12}, $5^{12}6^2$, $5^{12}6^3$, $5^{12}6^4$, $4^15^{10}6^2$, and $4^15^{10}6^3$ cages in PMH with d = 8 nm subjected to $\omega\tau_0$ = 1.0× 10^{-2} -1.0 × 10^{-4} at T = 270 K, as well as loading-free condition. (D) and (E) Changes in the percentage of sI and sII phase hydrates in PMHs with d = 8 and 14 nm subjected to $\omega\tau_0$ = 1.0 × 10^{-4} at T = 240 - 290 K. (F) The number of 5^{12}, $5^{12}6^2$, $5^{12}6^3$, $5^{12}6^4$, $4^15^{10}6^2$, and $4^15^{10}6^3$ cages in PMH with d = 8 nm at T = 240 -290 K subjected to $\omega\tau_0$ = 1.0 × 10^{-3}, as well as loading-free condition. (G) Perspective snapshot of PMH with d = 8 nm, in which the color code is based on the type of hydrate phase. Snapshots (1) and (2) of PMH with d = 8 nm subjected to $\omega\tau_0$ = 1.0× 10^{-2} and 1.0 × 10^{-4} at T = 270 K, while snapshots (3) and (4) of PMH with d = 14 nm subjected to T = 240 and 290 K at $\omega\tau_0$ = 1.0× 10^{-3}. Broken y-axes are used in panels a, b, d, and e to account for the large disparity in the fractions of sI and sII phases and to enhance the visibility of variations in the less abundant sII phase.

The dynamic mechanical behaviors and microstructural evolution of PMHs with different d subjected to high $\omega\tau_0$ = 0.1 at T = 270 K are uniquely exam-

ined. Figure 7A presents distribution of σ_{vm} in PMHs with d = 8 - 17 nm subjected to zero-shear strain. Resembling of the profile of E_w, the thickness of GBs in PMHs is independent on d. In the distribution curves of σ_{vm}, two peaks are identified, mainly corresponding to the stress of water particles in $5^{12}6^2$ and 5^{12} cages within grains. With increasing d, the two peaks of σ_{vm} become sharper and the probability distribution of water particles under high stress at the GBs.

Figure 7B compares the distributions of σ_{vm} of water particle in 5^{12}, $5^{12}6^2$, $5^{12}6^3$, $5^{12}6^4$, $4^15^{10}6^2$, and $4^15^{10}6^3$ cages in PMHs with d = 8 and 14 nm. For unconventional cages at GBs, the distributions of σ_{vm} of water particle in each unconventional cage in PMHs with d = 8 and 14 nm are similar, indicating that PMHs have similar loading stress states at GBs. Figure 7C shows side-viewed snapshots of localized PMH with d = 14 nm, in which the color code is based on the values of σ_{vm}. It is observed that significant stress concentration situates at those unconventional cages in GBs. Figure 7D presents the σ curves of PMHs with d = 8 - 17 nm subjected to cyclic shearing. As is seen, the σ curves are not perfect sinusoidal changes, differing from those subjected to low ω. By comparing, PMHs with smaller d yield larger σ_0. Figures 7E&F display the percentage of sI phase and the number of 5^{12} and $5^{12}6^2$ cages that are the components of sI hydrate phase in PMHs with d = 8 - 17 nm subjected to cyclic shearing. It is evident that PMHs with larger d have larger percentage of sI phase hydrate.

Figure 7G shows side-viewed configurations of PMHs with d = 8 and 14 nm at shear loading phases, in which the color code is on the basis of the type of cages. Subjected to the first shear loading cycle from 0 to 2π, PMHs with smaller d tend to destruct earlier and yield higher σ at failure. PMHs with d = 8 and 11 nm fail during the forward shearing (from 0 to π), while those with d = 14 and 17 nm fracture during the reverse shearing (from π to 2π). From Figures 7G(1)&(2), it is revealed that when the critical σ is imposed, cages at GBs destruct to form cracks, followed by crack propagation along the shearing direction. This causes failure of crystalline grains, which corresponds to the first drop in the sI phase percentage. Intriguingly, when the first loading cycle terminates, cracked grains recover, while the failures of GBs structures are irreversible. As a result, the percentage of sI hydrate phase and the number of cages rebound. Because PMHs with smaller d possess higher proportion of GBs, they tend to fail more severely, resulting in less rebound in the sI hydrate phase percentage and cage numbers.

During the second loading cycle from 2π to 4π, cages at GBs are further damaged, and cracks propagate from GBs to crystalline grains, leading to the second drop in sI hydrate phase and cage numbers. Interestingly, Figures 7G(4)&(5) reveal that, in PMH with d = 8 nm, cracks in grains do not disappear but produce transcrystalline fractures, initiating large-scale dissociation of PMHs. In contrast, when external σ exceed critical value in PMH with d = 14 nm, crystalline grains experience local elastic bending deformations which is called as kink banding. This type of deformation stores-imposed shear strain energy, thereby preventing fracture of grains, as illustrated by the yellow lines in Figure 7G(6). At GB junctions in PMHs with large d, cages undergo extensive dissociation, generating intergranular fractures. The grains in PMHs suffer extensive damage, explaining why σ_0 sharply increases during the second loading cycle. Whereas for PMHs with small d, transcrystalline fractures require greater σ.

In this work, we conduct in-depth investigation on the dynamic mechanics of PMHs under cyclic shearing loads, which mimic the stress fluctuations encountered during real-world energy extraction. Depending on ω, two distinct deformation regimes in PMHs are identified, covering the overall picture of dynamic mechanics. The d-ω dependency reveals a hierarchy of deformation mechanisms, namely, d governs microstructural failure pathways, while ω dictates the time scale of stress application relative to molecular relaxation. As schematically illustrated in Figure 8A, these behaviors are represented by two mechanical analog models (I and II), which capture the dominant deformation mechanisms at high and low frequencies, respectively.

At high ω (Model I in Figure 8A, $\omega\tau_0$ = 0.1), PMHs exhibit elasto-plastic deformation governed by a parallel combination of elastic and plastic elements. This behavior aligns with the Bingham model,[73-77] where high ω loading suppresses viscous dissipation, forcing deformation through instantaneous elastic strain and irreversible plastic slip. Subjected to cyclic shear, PMHs with smaller d yield larger σ_0, a trend analogous to the Hall-Petch effect in metals but driven by different mechanisms that GB strengthening in PMHs arises from increased intergranular frictional resistance rather than dislocation pile-ups in metals. Unlike metals, PMHs' molecular crystal nature of weak vdW-bonding between cages limits dislocation mobility, making GB sliding the primary plastic mechanism at small d. When d is critically small, failure occurs via transgranular fractures, whereas critically large d promotes intragranular kinking, reducing σ_0 and mitigating transgranular failure. Additionally, GB structures decompose under cyclic shear, enabling irreversible crack propagation along GBs, manifesting as intergranular plastic deformation. This highlights GBs as weak zones in PMHs, underscoring grain growth during hydrate formation dictate reservoir durability.

As ω decreases (Model II in Figure 8A, $\omega\tau_0$ < 0.02), PMHs exhibit pronounced viscoelasticity, governed by time-dependent processes. Lower ω allows sufficient time for molecular rearrangements, activating slow relaxation mechanisms such as GB sliding and cage network reconfiguration. Under low ω and elevated T, analyses of internal diffusion, GBs sliding, cage structure transitions, and sI ↔ sII hydrate phase transitions reveal that GB composition (e.g., amorphous vs. crystalline interfaces) dominates rheological behavior, driving the elastic-to-viscoelastic transition. Amorphous GBs have higher free volume, facilitating diffusion-driven creep, while crystalline GBs with ordered interfaces resist deformation.

The mechanical loss factor tan δ versus reduced $\omega\tau_0$ for PMHs is well-described by the Cross model. The applicability of Cross model confirms PMHs exhibit shear-thinning viscoelasticity, indicating a moderate transition from elastic to viscous behavior. Time-temperature superposition is observed in dynamic modulus spectra, where shifting ω spectra by a temperature-dependent factor collapses the data onto a master curve, validating the thermo-rheological simplicity of PMHs.

PMHs display distinct mechanical loss factor tan δ compared to supramolecular hydrogel, supramolecular polymer networks (SPN) and SPN-3[78-80] (Figure 8B) that show fascinating dynamic features such as self-healing, reversibility, and stimuli-responsiveness. Supramolecular materials rely on reversible non-covalent interactions (e.g., H-bonds, π-π stacking), while PMHs feature semi-permanent water cages held by H-bonds and guest molecules via vdW forces. For SPN and SPN-3, a rubber-like plateau (tan δ < 1.0) occurs at $\omega = 10^{-1}$-10^3 rad/s, reflecting dominant elastic behavior from network entanglement. As ω reduces, tan δ approaches 1.0, triggering a solid-to-fluid transition due to reversible bond dissociation. PMHs lack such reversible bonding, explaining their higher elastic plateau and slower tan δ increase with decreasing ω. Supramolecular hydrogels show tan δ > 1 at high $\omega = 10^3$-10^4 rad/s, characteristic of viscous liquid, transitioning to solid-like behavior at low ω due to network reformation. In contrast, PMHs exhibit a nonlinear tan δ increase with decreasing ω, transitioning gradually from elasticity to viscoelasticity. Extrapolating via the Cross model, PMHs exhibit a limiting tan δ value of approximately 0.22 at low ω, which is significantly lower than that of typical supramolecular materials, indicating a comparatively weaker dissipative (viscoelastic) response. This value is consistent with the generally low mechanical damping reported for crystalline ice materials, where internal friction remains limited due to the dominance of slow dissipation mechanisms such as grain boundary sliding and diffusion creep.

Following the signing of the Paris Agreement in 2016, carbon neutrality has become a central global challenge, drawing increasing attention to strategies that combine clean energy production with CO_2 sequestration in hydrate-bearing sediments. In this context, a low tan δ is of particular importance, as it reflects the ability of the system to maintain structural integrity under long-term, low-frequency perturbations. Although the present analysis focuses on methane hydrates, the fundamental mechanisms governing mechanical loss behavior, such as GB-mediated dissipation, cage distortion, and the progressive transition from elastic to viscoelastic response, are primarily controlled by the polycrystalline framework and interfacial dynamics. These features are therefore expected to be qualitatively transferable to CO_2 hydrates, which share similar clathrate structures and multiphase characteristics. Nevertheless, differences in guest molecule properties may lead to distinct quantitative responses. Compared with CH_4, CO_2 exhibits stronger guest–host interactions and a linear molecular geometry, which can influence cage stability, phase equilibria, and local rearrangement pathways. As a result, CO_2 hydrates may display higher structural rigidity and potentially modified dissipation

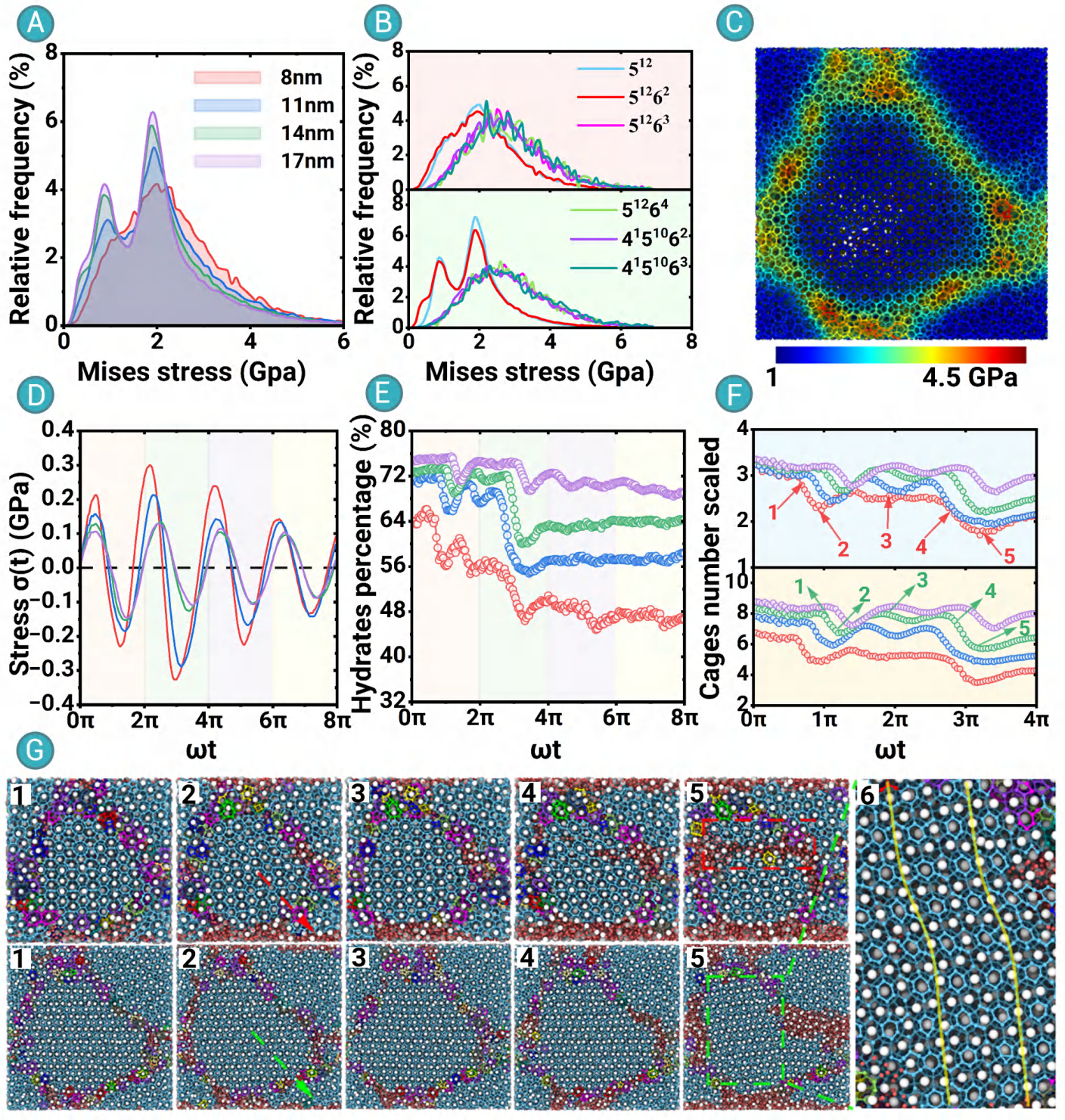

Figure 7. Dynamic mechanical properties and microstructural evolution of polycrystalline methane hydrates (PMHs) (A) Distribution of von Mises stress (σ_{vm}) of water particles in PMHs with d = 8 - 17 nm. (B) Distribution of σ_{vm} of water particles in 5^{12}, $5^{12}6^2$, $5^{12}6^3$, $5^{12}6^4$, $4^15^{10}6^2$, and $4^15^{10}6^3$ cages in PMHs with d = 8 - 17 nm. (C) Side-view of PMH with d = 14 nm, in which the color code is based on the values of σ_{vm}. (D) Variation in the σ in PMHs with d = 14 nm subjected to high $\omega\tau_0$ = 0.1 at T = 270 K. (E) and (F) The percentage of sI phase and the number of 5^{12} and $5^{12}6^2$ cages in PMHs with d = 8 - 17 nm subjected to high $\omega\tau_0$ = 0.1 at T = 270 K, respectively. (G) Side-viewed snapshots of PMHs with d = 8 and 14 nm subjected to high $\omega\tau_0$ = 0.1 at T = 270 K.

pathways under cyclic loading, thereby altering the frequency dependence of tan δ. Despite these differences, the relatively low tan δ limit predicted for polycrystalline methane hydrates suggests that hydrate-based systems can effectively preserve mechanical integrity under low-frequency disturbances. This characteristic is highly advantageous for long-term geological stability, supporting the feasibility of coupling methane recovery with CO_2 sequestration in hydrate reservoirs.

CONCLUSION

We comprehensively characterize the dynamic mechanical behaviors of PMHs under cyclic shear loading via MD simulations, revealing how d, T, and ω collectively govern two distinct deformation regimes. At high ω, PMHs exhibit elastoplastic behavior, where small-grained systems fail via transgranular fracture, while large-grained PMHs develop intragranular kink bands that enhance structural resilience through elastic bending. This d-dependent

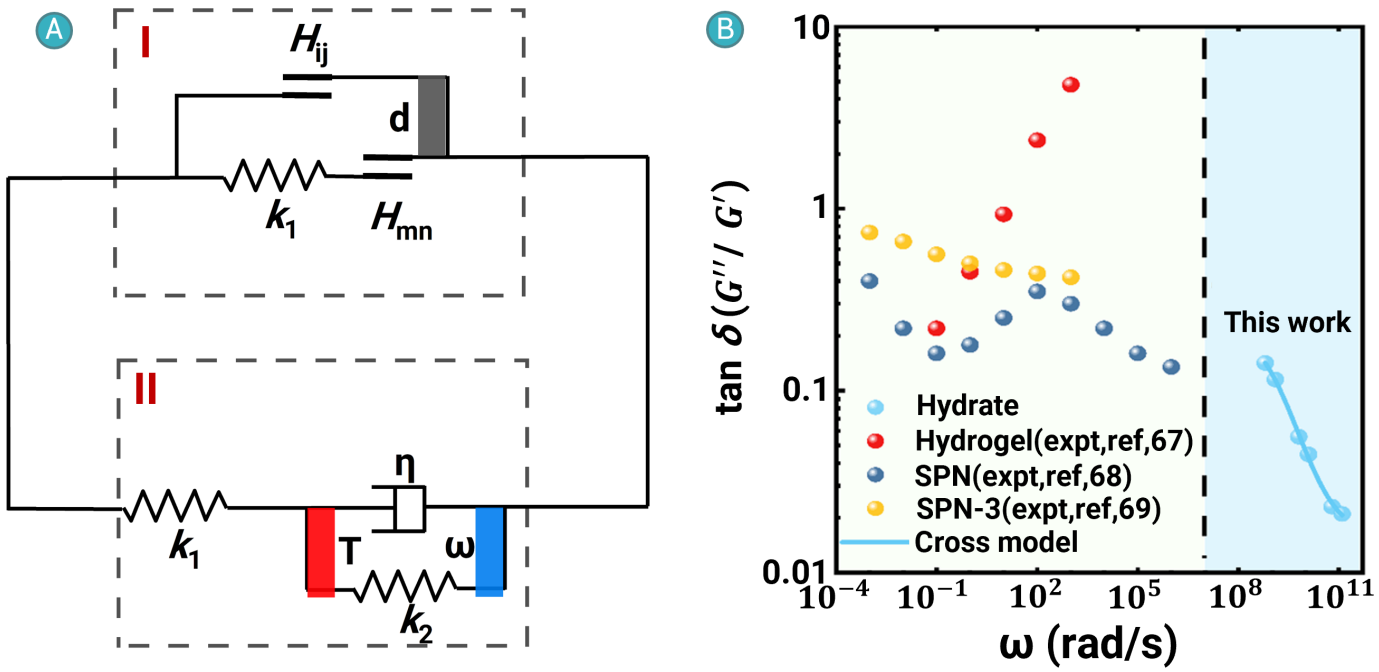

Figure 8. (A) Schematic of mechanical model for PMHs. Two mechanical modes are defined: Mode I (high-frequency, $\omega\tau_0 \approx 0.1$), represented by a parallel elastic-plastic model capturing solid-like elasto-plastic response; and Mode II (low-frequency, $\omega\tau_0 < 0.02$), incorporating viscous elements to describe viscoelastic deformation with enhanced time-dependent processes. k_1 and k_2 represent the elastic modulus of the grains and the GBs of PMHs, respectively. η is the coefficient of viscosity at the GBs. H_{ij} and H_{mn} are the initial frictional resistance of the grains and the GBs, respectively. d and T represent the grain size and temperature. ω represents the frequency. (B) Loss tangent frequency spectrum of PMHs, as well as other materials including supramolecular hydrogel,[78] SPN,[79] and SPN-3.[80]

mechanical response parallels the Hall-Petch relationship in metallic systems yet originates from the unique molecular-scale characteristics of gas hydrates, such as weak vdW bonding and restricted dislocation activity.

Under low ω/high T conditions, PMHs transition to viscoelastic regime dominated by GB-mediated processes. Key dissipation mechanisms include: (1) accelerated diffusion of water and methane molecules along GBs; (2) local cage transformations, notably between $5^{12}6^2$ and $4^15^{10}6^2$ cages; and (3) sI ↔ sII phase transitions. These molecular- to meso-scale processes collectively enable efficient strain energy dissipation and follow t- T superposition principles. The mechanical loss spectra are well captured by the Cross model for non-Newtonian fluids, with G'' exhibiting a characteristic power-law dependence on ω.

GBs serve as critical hotspots for mechanical dissipation, enriched with metastable cage structures that readily reorganize under stress. The nonlinear relationships among d, ω, and dynamic moduli indicate that fine-grained PMHs are more prone to mechanical instability, which is an insight with direct implications for hydrate-bearing sediments, where reduced grain cementation is linked to enhanced landslide susceptibility. By establishing cross-scale linkages between cage-level dynamics, GB processes, and macroscale viscoelasticity, this study provides a mechanistic framework for predicting the long-term NGH reservoir stability under tectonic or anthropogenic stresses. These insights can contribute to risk assessment in NGH exploitation and inform the design of CO_2 sequestration strategies in hydrate-rich formations.

REFERENCES

1. Sloan E. (2003). Fundamental principles and applications of natural gas hydrates. *Nat.* **426**:353–359. DOI:10.1038/nature02135
2. Koh C. (2002). Towards a fundamental understanding of natural gas hydrates. *Chem. Soc. Rev.* **31**:157–167. DOI:10.1039/b008672j
3. Walsh M., Koh C., Sloan E., et al. (2009). Microsecond Simulations of Spontaneous Methane Hydrate Nucleation and Growth. *Sci.* **326**:1095–1098. DOI:10.1126/science.1174010

Abbreviations

NGHs	Natural gas hydrates
HB	Hydrogen-bonded
PMHs	Polycrystalline methane hydrates
MHs	Methane hydrates
MD	Molecular dynamics
GB	Grain-boundary
d	Grain size
T	Temperature
ω	Loading frequency
VTA	Voronoi tessellation algorithm
PBCs	Periodic boundary conditions
mW	Monatomic water
SW	Stillinger-Weber
NPT	Constant number of particles, constant pressure, and constant temperature
NVT	Constant number of particles, constant volume, and constant temperature
HTR	Hierarchical Topological Ring
HTB	High-temperature background
MSD	Mean square displacements
D	Diffusion coefficients
SPN	Supramolecular polymer networks

4. Jacobson L., Hujo W. and Molinero V. (2010). Amorphous Precursors in the Nucleation of Clathrate Hydrates. *J. Am. Chem. Soc.* **132**:11806–11811. DOI:10.1021/ja1051445
5. Cox S., Taylor D., Youngs T., et al. (2018). Formation of Methane Hydrate in the Presence of Natural and Synthetic Nanoparticles. *J. Am. Chem. Soc.* **140**:3277–3284. DOI:10.1021/jacs.7b12050
6. Strobel T., Hester K., Sloan E., et al. (2007). A Hydrogen Clathrate Hydrate with Cyclohexanone: Structure and Stability. *J. Am. Chem. Soc.* **129**:9544–9545. DOI:10.1021/ja072074h
7. Kvenvolden K. (1993). Gas Hydrates - Geological Perspective and Global Change. *Rev. Geophys.* **31**:173–187. DOI:10.1029/93rg00268
8. Kvenvolden K. (1988). Methane Hydrate - a Major Reservoir of Carbon in the Shallow Geosphere. *Chem. Geol.* **71**:41–51. DOI:10.1016/0009-2541(88)90104-0
9. Lu H., Seo Y., Lee J., et al. (2007). Complex gas hydrate from the Cascadia margin. *Nat.* **445**:303–306. DOI:10.1038/nature05463
10. Moon C., Taylor P. and Rodger P. (2003). Molecular Dynamics Study of Gas Hydrate Formation. *J. Am. Chem. Soc.* **125**:4706–4707. DOI:10.1021/ja028537v
11. Max M. and Clifford S. (2000). The state, potential distribution, and biological implications of methane in the Martian crust. *J Geophys. Res. Planet.* **105**:4165–4171. DOI:10.1029/1999je001119
12. Loveday J., Nelmes R., Guthrie M., et al. (2001). Stable methane hydrate above 2 GPa and the source of Titan's atmospheric methane. *Nat.* **410**:661–663. DOI:10.1038/35070513
13. Lunine J. and Stevenson D. (1985). Thermodynamics of Clathrate Hydrate at Low and High-Pressures with Application to the Outer Solar-System. *Astrophys. J. Suppl. Ser.* **58**:493–531. DOI. DOI:10.1086/191050
14. Phrampus B. and Hornbach M. (2012). Recent changes to the Gulf Stream causing widespread gas hydrate destabilization. *Nat.* **490**:527–531. DOI:10.1038/nature11528
15. Hesselbo S., Gröcke D., Jenkyns H., et al. (2000). Massive dissociation of gas hydrate during a Jurassic oceanic anoxic event. *Nat.* **406**:392–395. DOI:10.1038/35019044
16. Ning F., Yu Y., Kjelstrup S., et al. (2012). Mechanical properties of clathrate hydrates: status and perspectives. *Energ Environ. Sci.* **5**:6779–6795. DOI:10.1039/c2ee03435b
17. Zhu J., Du S., Yu X., et al. (2014). Encapsulation kinetics and dynamics of carbon monoxide in clathrate hydrate. *Nat. Commun.* **5**:4128. DOI:10.1038/ncomms5128
18. Durham W., Kirby S., Stern L., et al. (2003). Correction to "The strength and rheology of methane clathrate hydrate". *J. Geophys. Res-Sol. Ea.* **108**:2182. DOI:10.1029/2003jb002534
19. Durham W., Stern L. and Kirby S. (2003). Ductile flow of methane hydrate. *Can. J. Phys.* **81**:373–380. DOI:10.1139/P03-042
20. Stern L., Kirby S. and Durham W. (1998). Polycrystalline methane hydrate: Synthesis from superheated ice, and low-temperature mechanical properties. *Energ. Fuel.* **12**:201–211. DOI:10.1021/ef970167m
21. Miyazaki K., Yamaguchi T., Sakamoto Y., et al. (2011). Time-dependent behaviors of methane-hydrate bearing sediments in triaxial compression test. *International Journal of the JCRM* **7**:43–48. DOI:10.11187/ijjcrm.7.43
22. Miyazaki K., Endo Y., Tenma N., et al. (2015). Constitutive Equation for Triaxial Compression Creep of Artificial Methane-Hydrate-Bearing Sand. *J. of Mmij* **131**:47–55. DOI:10.2473/journalofmmij.131.47
23. Miyazaki K., Tenma N. and Yamaguchi T. (2017). Relationship between Creep Property and Loading-Rate Dependence of Strength of Artificial Methane-Hydrate-Bearing Toyoura Sand under Triaxial Compression. *Energies* **10**:1466. DOI:10.3390/en10101466
24. Wu J., Ning F., Trinh T., et al. (2015). Mechanical instability of monocrystalline and polycrystalline methane hydrates. *Nat. Commun.* **6**:8743. DOI:10.1038/ncomms9743
25. Cao P., Sheng J., Wu J., et al. (2021). Mechanical creep instability of nanocrystalline methane hydrates. *Phys. Chem. Chem. Phys.* **23**:3615–3626. DOI:10.1039/d0cp05896c
26. Wang K., Hu Y. and He J. (2012). Deformation cycles of subduction earthquakes in a viscoelastic Earth. *Nat.* **484**:327–332. DOI:10.1038/nature11032
27. Mitsui Y., Muramatsu H. and Tanaka Y. (2021). Slow deformation event between large intraslab earthquakes at the Tonga Trench. *Sci. Rep.* **11**:257. DOI:10.1038/s41598-020-80728-w
28. Wang M., Barnes P., Morgan J., et al. (2023). Compactive deformation of incoming calcareous pelagic sediments, northern Hikurangi subduction margin, New Zealand: Implications for subduction processes. *Earth Planet Sci. Lett.* **605**:118022. DOI:10.1016/j.epsl.2023.118022
29. Wang K. and Bilek S. (2011). Do subducting seamounts generate or stop large earthquakes. *Geology* **39**:819–822. DOI:10.1130/g31856.1
30. Morris S. and Jackson I. (2009). Diffusionally assisted grain-boundary sliding and viscoelasticity of polycrystals. *Mech. Phys. Solids* **57**:744–761. DOI:10.1016/j.jmps.2008.12.006
31. Lee L. and Morris S. (2010). Anelasticity and grain boundary sliding. *P. Roy. Soc. A-Math. Phy.* **466**:2651–2671. DOI:10.1098/rspa.2009.0624
32. Lee L., Morris S. J. and Wilkening J. (2011). Stress concentrations, diffusionally accommodated grain boundary sliding and the viscoelasticity of polycrystals. *P. Roy. Soc. A-Math. Phy.* **467**:1624–1644. DOI:10.1098/rspa.2010.0447
33. Duan C. and Wei Y. (2020). Scaling of internal dissipation of polycrystalline solids on grain-size and frequency. *Acta Mater.* **201**:350–363. DOI:10.1016/j.actamat.2020.10.004
34. Hirel P. (2015). Atomsk: A tool for manipulating and converting atomic data files. *Comput. Phys. Commun.* **197**:212–219. DOI:10.1016/j.cpc.2015.07.012
35. McMullan R. and Jeffrey G. (1965). Polyhedral Clathrate Hydrates. *IX. Structure of Ethylene Oxide Hydrate. J. Chem. Phys.* **42**:2725–2732. DOI:10.1063/1.1703228
36. Molinero V. and Moore E. (2009). Water Modeled As an Intermediate Element between Carbon and Silicon. *J. Phys. Chem. B* **113**:4008–4016. DOI:10.1021/jp805227c
37. Jacobson L. and Molinero V. (2010). A Methane-Water Model for Coarse-Grained Simulations of Solutions and Clathrate Hydrates. *J. Phys. Chem. B* **114**:7302–7311. DOI:10.1021/jp1013576
38. Jacobson L., Hujo W. and Molinero V. (2009). Thermodynamic Stability and Growth of Guest-Free Clathrate Hydrates: A Low-Density Crystal Phase of Water. *J. Phys. Chem. B* **113**:10298–10307. DOI:10.1021/jp903439a
39. Jacobson L., Hujo W. and Molinero V. (2010). Nucleation Pathways of Clathrate Hydrates: Effect of Guest Size and Solubility. *J. Phys. Chem. B* **114**:13796–13807. DOI:10.1021/jp107269q
40. Nguyen A. and Molinero V. (2014). Cross-nucleation between clathrate hydrate polymorphs: Assessing the role of stability, growth rate, and structure matching. *J. Chem. Phys.* **140**:3440. DOI:10.1063/1.4866143
41. Liu Y., Xu K., Xu Y., et al. (2022). HTR: An ultra-high speed algorithm for cage recognition of clathrate hydrates. *Nanotechnol. Rev.* **11**:699–711. DOI:10.1515/ntrev-2022-0044
42. Shi Q., Lin Z., Qu Y., et al. (2024). HTR plus : a novel algorithm for identifying type and polycrystal of gas hydrates. *J. Phys-Condens. Mat.* **36**:365901. DOI:10.1088/1361-648X/ad52df
43. Walsh M., Rainey J., Lafond P., et al. (2011). The cages, dynamics, and structuring of incipient methane clathrate hydrates. *Phys. Chem. Chem. Phys.* **13**:19951–19959. DOI:10.1039/c1cp21899a
44. Xu K., Ma R., Qu Y., et al. (2025). Grain boundary strength in methane hydrates. *Pet. Sci.* **22**:5268–5276. DOI:10.1016/j.petsci.2025.10.018
45. Li X., Huang J., Xiong K., et al. (2025). CO_2 sequestration trade-offs in polycrystalline hydrate stability. *CN* **4**. DOI:10.1007/s43979-025-00151-w.
46. Peng Y., Liu H., Xin Y., et al. (2021). Rheological conductor from liquid metal-polymer composites. *Matter* **4**:3001–3014. DOI:10.1016/j.matt.2021.06.046
47. Luo W., Wang C., Hu X., et al. (2012). Long-Term Creep Assessment of Viscoelastic Polymer by Time-Temperature-Stress Superposition. *Acta Mech. Solida Sin.* **25**:571–578. DOI:10.1016/S0894-9166(12)60052-4
48. Ding Y. and Sokolov A. (2006). Breakdown of time-temperature superposition principle and universality of chain dynamics in polymers. *Macromolecules* **39**:3322–3326. DOI:10.1021/ma052607b
49. Krauklis A., Akulichev A., Gagani A., et al. (2019). Time-Temperature-Plasticization Superposition Principle: Predicting Creep of a Plasticized Epoxy. *Polymers* **11**:1848. DOI:10.3390/polym11111848
50. Xie J. and Jin Y. (2016). Parameter determination for the Cross rheology equation and its application to modeling non-Newtonian flows using the WC-MPS method. *Eng. Appl. Comp. Fluid.* **10**:111–129. DOI:10.1080/19942060.2015.1104267
51. Hauswirth S., Bowers C., Fowler C., et al. (2020). Modeling cross model non-Newtonian fluid flow in porous media. *J. Contam. Hydrol.* **235**:103708. DOI:10.1016/j.jconhyd.2020.103708
52. Hafeez A., Yasir M., Khan M., et al. (2021). Buoyancy effect on the chemically reactive flow of Cross nanofluid over a shrinking surface: Dual solution. *Int. Commun. Heat. Mass.* **126**:105438. DOI:10.1016/j.icheatmasstransfer.2021.105438
53. Nowick A. and Berry B. (1972). Anelastic relaxation in crystalline solids (Academic Press).
54. Jackson I., Faul U., Fitz Gerald J., et al. (2006). Contrasting viscoelastic behavior of melt-free and melt-bearing olivine: Implications for the nature of grain-boundary sliding. *Mat. Sci. Eng. A-Struct.* **442**:170–174. DOI:10.1016/j.msea.2006.01.136
55. Barnhoorn A., Jackson I., Gerald J., et al. (2007). Suppression of elastically accommodated grain-boundary sliding in high-purity MgO. *J. Eur. Ceram. Soc.* **27**:4697–4703. DOI:10.1016/j.jeurceramsoc.2007.04.005
56. Pezzotti G., Kleebe H. and Ota K. (1998). Grain-boundary viscosity of polycrystalline silicon carbides. *J. Am. Ceram. Soc.* **81**:3293–3299. DOI:10.1111/j.1151-2916.1998.tb02770.x
57. Pezzotti G., Kleebe H., Ota K., et al. (2005). Suppression of Viscous Grain - Boundary Sliding in a Dilute SiAlON Ceramic. *J. Am. Ceram. Soc.* **80**:2349–2354. DOI:10.1111/j.1151-2916.1997.tb03126.x
58. Mosher D. and Raj R. (1974). Use of the internal friction technique to measure rates of grain boundary sliding. *Acta Metall.* **22**:1469–1474. DOI:10.1016/0001-6160(74)90108-4
59. Kim B., Hiraga K. and Morita K. (2005). Viscous grain-boundary sliding and grain rotation accommodated by grain-boundary diffusion. *Acta Materialia* **53**:1791–1798. DOI:10.1016/j.actamat.2004.12.028
60. Liu J., Fu R., Lin Y., et al. (2022). Mechanical Destabilization and Cage Transformations in Water Vacancy-Contained CO Hydrates. *Acs Sustainable Chem. Eng.* **10**:10339–10350. DOI:10.1021/acssuschemeng.2c03072
61. Bulatov V., Hsiung L., Tang M., et al. (2006). Dislocation multi-junctions and strain hardening. *Nat.* **440**:1174–1178. DOI:10.1038/nature04658

62. Sendrowicz A., Myhre A., Danyuk A., et al. (2022). Dislocation kinetics explains energy partitioning during strain hardening: Model and experimental validation by infrared thermography and acoustic emission. *Mat. Sci. Eng. A-Struct.* **856**:143969. DOI:10.1016/j.msea.2022.143969
63. Freund L. (1994). The Mechanics of Dislocations in Strained-Layer Semiconductor-Materials. *Adv. Appl. Mech.* **30**:1–66. DOI:10.1016/S0065-2156(08)70173-X
64. Li C., Liu K., Jiang D., et al. (2023). Pressure - Driven Polymorphic Transition, Emergent Insulator - To - Metal Transition, and Photoconductivity Switching in Violet Phosphorus. *Small* **20**:e2306758. DOI:10.1002/smll.202306758
65. Wu K., Yang Y. and Gao L. (2020). A review on phase transition and structure-performance relationship of second-order nonlinear optical polymorphs. *Coord. Chem. Rev.* **418**:213380. DOI:10.1016/j.ccr.2020.213380
66. Chou I., Sharma A., Burruss R., et al. (2000). Transformations in methane hydrates. *Proc. Natl. Acad. Sci.* **97**:13484–13487. DOI:10.1073/pnas.250466497
67. Ikeda T. and Terakura K. (2003). Structural transformation of methane hydrate from cage clathrate to filled ice. *J. Chem. Phys.* **119**:6784–6788. DOI:10.1063/1.1606437
68. Sun Q., Duan T., Zheng H., et al. (2005). Phase transformation of methane hydrate under high pressure. *J. Chem. Phys.* **122**:024714. DOI:10.1063/1.1830411
69. Tanaka T., Hirai H., Matsuoka T., et al. (2013). Phase changes of filled ice Ih methane hydrate under low temperature and high pressure. *J. Chem. Phys.* **139**:104701. DOI:10.1063/1.4820358
70. Kadobayashi H., Hirai H., Ohfuji H., et al. (2020). Structural evolution of methane hydrate under pressures up to 134 GPa. *J. Chem. Phys.* **152**:194308. DOI:10.1063/5.0007511
71. Halpern Y., Thieu V., Henning R., et al. (2001). Time-resolved in situ neutron diffraction studies of gas hydrate: Transformation of structure II (sII) to structure I (sI). *J. Am. Chem. Soc.* **123**:12826–12831. DOI:10.1021/ja010280y
72. Schicks J., Naumann R., Erzinger J., et al. (2006). Phase transitions in mixed gas hydrates: Experimental observations versus calculated data. *J. Phys. Chem. B* **110**:11468–11474. DOI:10.1021/jp0612580
73. Montassar S. and de Buhan P. (2006). A numerical model to investigate the effects of propagating liquefied soils on structures. *Comput. Geotech.* **33**:108–120. DOI:10.1016/j.compgeo.2006.02.003
74. Marr J., Elverh$i A., Harbitz C., et al. (2002). Numerical simulation of mud-rich subaqueous debris flows on the glacially activemargins of the Svalbard–Barentssea. *Mar. Geol.* **188**:351–364. DOI:10.1016/S0025-3227(02)00310-9
75. Luna B., Remaître A., van Asch T., et al. (2012). Analysis of debris flow behavior with a one dimensional run-out model incorporating entrainment. *Eng. Geol.* **128**:63–75. DOI:10.1016/j.enggeo.2011.04.007
76. Hadush S., Yashima A., Uzuoka R., et al. (2001). Liquefaction induced lateral spread analysis using the CIPmethod. *Comput. Geotech.* **28**:549–574. DOI:10.1016/S0266-352X(01)00016-7
77. Geertsema M., Hungr O., Schwab J., et al. (2006). A large rockslide–debris avalanche in cohesive soil at Pink Mountain, northeastern British Columbia, Canada. *Eng. Geol.* **83**:64–75. DOI:10.1016/j.enggeo.2005.06.025
78. Hafeez S., Decarli M., Aldana A., et al. (2023). In Situ Covalent Reinforcement of a Benzene-1,3,5-Tricarboxamide Supramolecular Polymer Enables Biomimetic, Tough, and Fibrous Hydrogels and Bioinks. *Adv. Mater.* **35**:e2301242. DOI:10.1002/adma.202301242
79. Deng J., Bai R., Zhao J., et al. (2023). Insights into the Correlation of Cross-linking Modes with Mechanical Properties for Dynamic Polymeric Networks. *Angew. Chem. Int. Edit.* **62**:e202309058. DOI:10.1002/anie.202309058
80. Liu Y., Wan J., Zhao X., et al. (2023). Highly Strong and Tough Supramolecular Polymer Networks Enabled by Cryptand-Based Host-Guest Recognition. *Angew. Chem. Int. Ed.* **62**:e202302370. DOI:10.1002/anie.202302370

FUNDING AND ACKNOWLEDGMENTS

This work is financially supported by the National Natural Science Foundation of China (Grant Nos. 12572127 and 12172314), and the 111 project (B16029). Zhiliang Zhang is grateful for the support of the Research Council of Norway through the Dandra project (Project No. 302348). The supercomputer GPU hours are provided by Shaorong Fang and Tianfu Wu from Information and Network Center of Xiamen University, and they are acknowledged for the help with the high-performance computer.

AUTHOR CONTRIBUTIONS

Yongxiao Qu: Methodology, Investigation, Formal analysis, Data curation, Writing – original draft. Qiao Shi: Conceptualization, Formal analysis, Software, Writing – original draft. Gaoyang Luo: Methodology, Formal analysis, Visualization. Rui Ma: Investigation, Formal analysis. Zhisen Zhang: Conceptualization, Formal analysis, Supervision, Resources. Zhiliang Zhang: Supervision, Formal analysis, Writing – review & editing. Jianyang Wu: Supervision, Funding acquisition, Resources, Methodology, Formal analysis, Writing – review & editing. All authors contributed to the manuscript and approved the final version.

DECLARATION OF INTERESTS

The authors declare no competing interests.

DATA AND CODE AVAILABILITY

Data are available from the corresponding author upon reasonable request.

SUPPLEMENTAL INFORMATION

It can be found online at https://doi.org/10.59717/j.xinn-energy.2026.100157.